IMPROVING THE PERFORMANCE OF THE SPACE SURVEILLANCE TELESCOPE AS A FUNCTION OF SEEING PARAMETER

THESIS

Jae H. Jeon, Captain, USAF

AFIT-ENG-MS-15-M-050

DEPARTMENT OF THE AIR FORCE
AIR UNIVERSITY

AIR FORCE INSTITUTE OF TECHNOLOGY

Wright-Patterson Air Force Base, Ohio

AFIT-ENG-MS-15-M-050

IMPROVING THE PERFORMANCE OF THE SPACE SURVEILLANCE TELESCOPE AS A FUNCTION OF SEEING PARAMETER

THESIS

Presented to the Faculty

Department of Electrical and Computer Engineering

Graduate School of Engineering and Management

Air Force Institute of Technology

Air University

Air Education and Training Command

In Partial Fulfillment of the Requirements for the

Degree of Master of Science in Electrical Engineering

Jae H. Jeon, BS

Captain, USAF

March 2015

AFIT-ENG-MS-15-M-050

IMPROVING THE PERFORMANCE OF THE SPACE SURVEILLANCE TELESCOPE AS A FUNCTION OF SEEING PARAMETER

Jae H. Jeon, B.S.E.E.

Captain, USAF

Committee Membership:

Dr. Stephen C. Cain
Chair

Lt. Colonel Travis F. Blake, Ph.D.
Member

Maj Milo W.. Hyde, PhD
Member

Abstract

This research paper investigates ways to improve the detection capability and predict the performance of the *Space Surveillance Telescope* (SST) system when it's relocated to Exmouth, Australia. The dataset collected by the SST observing the *Geosynchronous Earth Orbit* (GEO) satellite, ANIK-F1, entering the earth's eclipse is used to test the performance of the three existing and one new detection algorithm. The three existing algorithms are the point detection (*Binary Hypothesis Test* (BHT)), correlation detection (CD-BHT), and *Multi-hypothesis Test using ten hypotheses* (MHT_{10}), and the new detection algorithm is the *Multi-hypothesis Test using six hypotheses* (MHT_6). To improve the accuracy and validness of the comparison, a new method of obtaining the true atmospheric seeing parameter, terminator (point before the object entering the eclipse), and parameters used for the comparison are also investigated. It is found that the MHTs vastly outperform the BHTs, and the MHT_6 offers a similar or improved performance over the MHT_{10}, but requiring only half of the computing power. Although, the detection performance is expected to suffer when SST is relocated to Exmouth, Australia from current location in Socorro New Mexico, but by implementing the new detection algorithms, the lost performance can be bought back and even improve beyond current performance level.

In addition, an AFIT telescope experiment is conducted to provide an additional set of measured data used to strengthen the fidelity of analytical model for calculating the and to test the SST's detection algorithms under very poor seeing conditions.

AFIT-ENG-MS-15-M-050

Acknowledgments

I would like to thank my cohorts in the electro-optics program for helping me throughout the AFIT program. I would like to express my sincere appreciation to my faculty advisor, Dr. Stephen Cain, for his guidance and support throughout the course of this thesis effort. I would, also, like to thank my sponsor, Lt Col Travis Blake, from the Executive Office of the President for both the insight and latitude provided to me in this research.

Jae H. Jeon

Table of Contents

Page

List of Figures

Figure **Page**

List of Tables

Table **Page**

List of Abbreviations

Abbreviation	
AFSPC	Air Force Space Command
AMOS	Air Force Optical and Supercomputing
BHT	Binary Hyothesis Test
CCD	Charged-Couple Device
DARPA	Defense Advanced Research Projects Agency
DGC	Deigo Garcia
DoD	Department of Defense
FOV	Field of View
GBO	Ground Based Optics
GEO	Geosynchronous Orbit
GEODDS	Ground-Based Electro-Optical Deep Space Surveillance System
HEO	Highly Elliptical Orbit
H-V	Hufnagal Valley
LEO	Low Earth Orbit
LINEAR	Lincoln Near Earth Asteroid Research
MEO	Medium Elliptical Orbit
MHT	Multi-Hyothesis Test
MHT_6	Multi-Hyothesis Test using six hypotheses
MHT_{10}	Multi-Hyothesis Test using ten hypotheses

MIT/LL	Massachusetts Institute of Technology Lincoln Lab
MLT	Maximum Likelihood Test
M&S	Modeling and Simulation
NASA	National Aeronautics and Space Administration
NEO	Near Earth Objects
OTF	Optical Transfer Fucntion
PDF	Probability Density Function
PSF	Point Spread Function
RADAR	RAdio Detection And Ranging
ROC	Receiver Operating Characteristic
SBO	Space Based Optics
SBSS	Space Based Space Surveillance
SDA	Space Domain Awareness
SMC	Space and Missile Center
SNR	Signa- to-Noise Ratio
SSA	Space Situational Awareness
SSN	Space Survillence Network
SST	Space Surveillance Telescope
UCT	UnCorrelated Targets
USNO	United States Naval Observatory

IMPROVING THE PERFORMANCE OF THE SPACE SURVEILLANCE TELESCOPE AS A FUNCTION OF SEEING PARAMETER

I. Introduction

1.1 General Issue

1.1.1 Contested Environment

Today, the skies over Earth are becoming an ever more congested and contested environment, where nations and commercial entities are competing for the prime real estate in Earth's GEO. In addition to domestic and international entities, emerging countries and threat countries are also embracing space systems, driven mainly by the relative expensiveness of placing the nano to mini-satellite into an orbit [1]. There are over 55 countries with active space programs as shown in Figure 1, and the numbers are expected only to rise [2]. Future markets in space systems are continuously growing with no sign of slowing down [3].

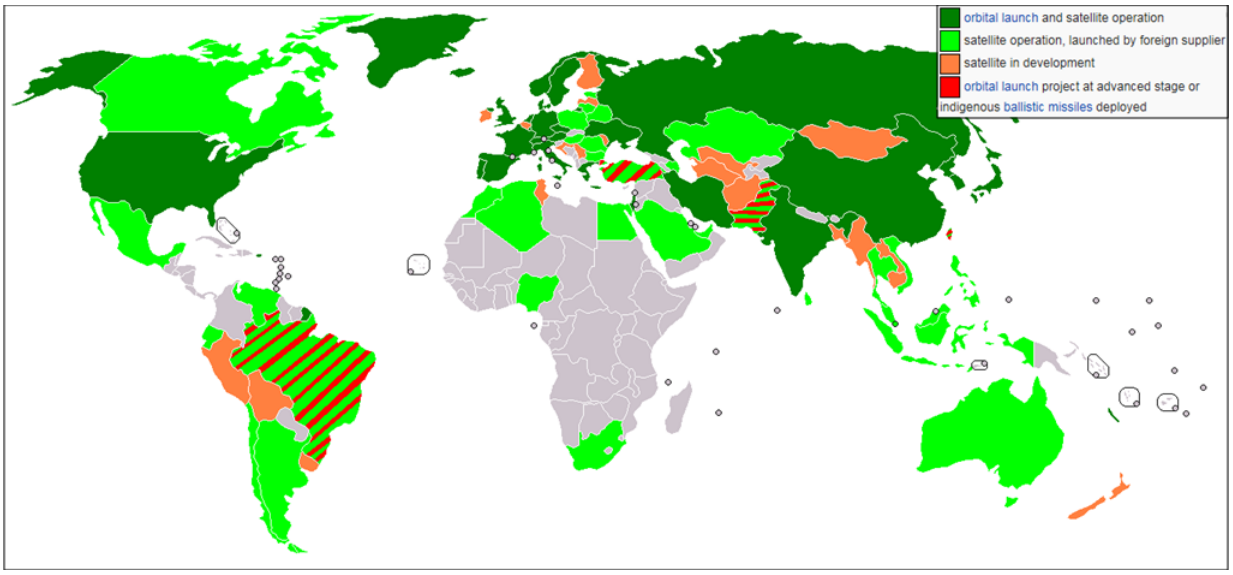

Figure 1. Countries with active space programs.

1.1.2 Orbital Hazards and Threats

As a result of the pursuit of space technologies, the Earth's orbits are now cluttered with thousands of space systems and hundreds of thousands of debris in various sizes. These space objects pose a significant threat to the key orbits and future space travel. Collision with small debris can cause minor damage to the space systems, but a larger debris or object can destroy and wreak havoc on a nearby orbit, which can also make it more hazardous or shrink usable orbits.

Those fears were realized and orbital conditions worsened with the Chinese Fengyun-1C anti-satellite test and the collision of Iridium-33 and Cosmos 2251. Two collisions significantly increased orbital debris in *Low Earth Orbit* (LEO), damaged nearby space systems, and rendered nearby orbits unusable [4, 5]. Both events demonstrated the danger of an intentional or unintentional orbital collision. The long term outlook is even more dire because according to the Rand Corporation, the number of objects in LEO that are one centimeter in size or larger are expected to grow by an order of many magnitudes when future explosions and collisions are modeled [6]. The prediction model is shown in Figure 2. It's important to note that the model doesn't incorporate future explosions or collisions occurring at non LEOs. Although the past two collisions took place in LEO, there is no guarantee that future collisions won't occur in more valuable orbits like in the *Medium Elliptical Orbit* (MEO), *Highly Elliptical Orbit* (HEO), or *Geosynchronous Orbit* (GEO). If the MEO, HEO, and GEO explosions and collisions are modeled in, orbital conditions are expected to be much worse.

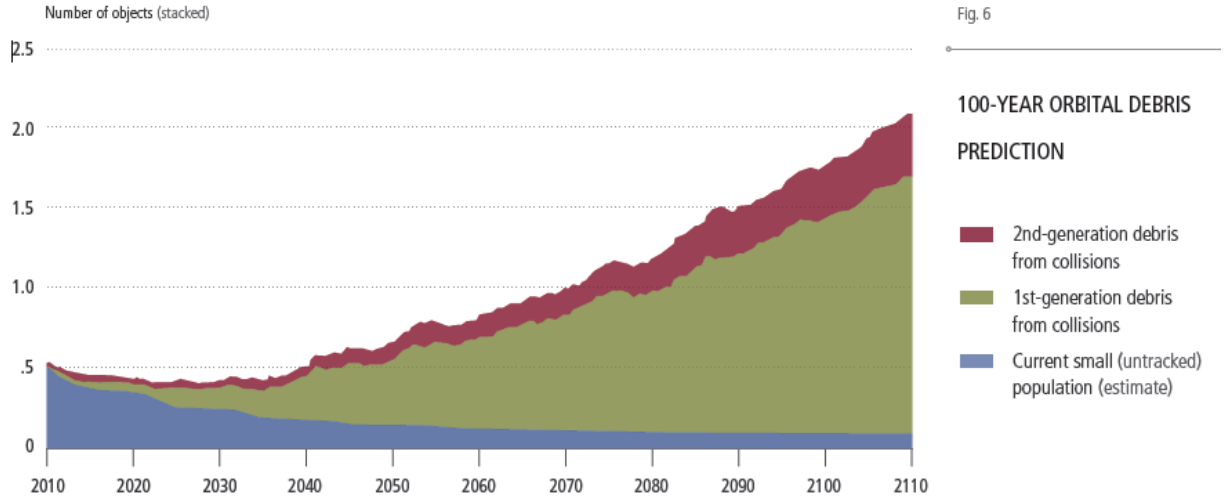

Figure 2. Predicted number of objects in low Earth orbit that are 1 cm in size or larger, by year over the next 100 years. The scenario assumes a continuation of recent launch rates and weak adherence to international debris mitigation standards. Spacecraft shielding is only feasible against debris smaller than 1 cm in size [6].

To better manage the space traffic, the United States Congress mandated the *National Aeronautics and Space Administration* (NASA) to identify major threats against the United States space assets and Earth [7, 8] [7, 8]. In collaboration with the *Department of Defense* (DoD), three major threats were identified. They are orbital debris, micro-satellites, and the *Near Earth Objects* (NEO). Two of three identified are threats against the space assets, hence it became even more crucial to detect and track orbital objects in order to avoid or mitigate possible intentional or unintentional orbital collisions in the future.

1.1.3 Space Situational Awareness

According to the U.S. National Space Policy, *Space Situational Awareness* (SSA) is a critical civilian and military mission that directly supports U.S. National Space Policy to "[p]reserve the Space Environment…the United States shall: Develop, maintain, and use space situational awareness information from commercial, civil, and national security sources to detect, identify, and attribute actions in space that are contrary to responsible use and the long-term

sustainability of the space environment; SSA information shall be used to support national and homeland security, civil space agencies, particularly human space flight activities, and commercial and foreign space operations [9]."

In accordance with the U.S. National Space Policy, the United States Strategic Command's crafted updated Space Control Joint Capabilities Document [10, 11]. Thus, DoD made the SSA a top priority with the goal of providing globally responsive SSA capability to detect, track, characterize, and identify all adversary and friendly space forces in Near-Real-Time [12]. This capability will provide and enable DoD with the ability to effectively maintain communication, overhead observation and other critical capabilities upon which military, civilian and commercial functions heavily rely [13].

Currently, the DoD employs three different technologies for conducting the SSA mission. Sensors include *Space Based Optics* (SBO), *Ground Based Optics* (GBO), and *RAdio Detection And Ranging* (RADAR). But, the use of the GBO has been considered by many to be the most cost efficient way of detecting objects in the GEO for following reasons. First, current RADAR systems like the Upgraded Early Warning Radars are mainly utilized by the Missile Defense Agency for the missile defense, early warning, SSA mission in the LEO and limited SSA mission in the GEO [14]. The SSA mission is conducted mainly in LEO due to the limitation (power versus search) of RADAR technology for its use in GEO [15, 16]. An ability to conduct the SSA mission in GEO is especially important for the USAF because the many of the DoDs high value assets and missions are conducted from the GEO belt. Second, despite being highly capable, the SBO is comparably an expensive system with estimated acquisition cost of $1 billion to field [17]. Furthermore, the *Space Based Space Surveillance* (SBSS) block 10 satellite is approaching the end of life sometime around 2017, but the follow-on efforts are delayed due to

the high acquisition cost. According to the SBSS Program Executive Officer, the SBSS follow-on is projected to be ready by 2022, leaving a five year gap [18]. However, this is best case scenario and the schedule can slip even further in the current fiscal environment. Additionally, because the SBO system like the SBSS is physically located in LEO, it suffers from risks associated with orbital debris and objects mentioned in Section 1.1.2.

1.1.4 Space Surveillance Telescope

Due to the sheer number of space objects in Earth's orbit as shown in Figure 3, legacy system's detection and tracking capability were saturated and as a result, often missed detecting or lost track of its target(s). These undetected, unknown, or lost space objects are known as *UnCorrelated Targets* (UCTs). A new system was desperately needed to detect and track the growing number of orbital objects and UCTs.

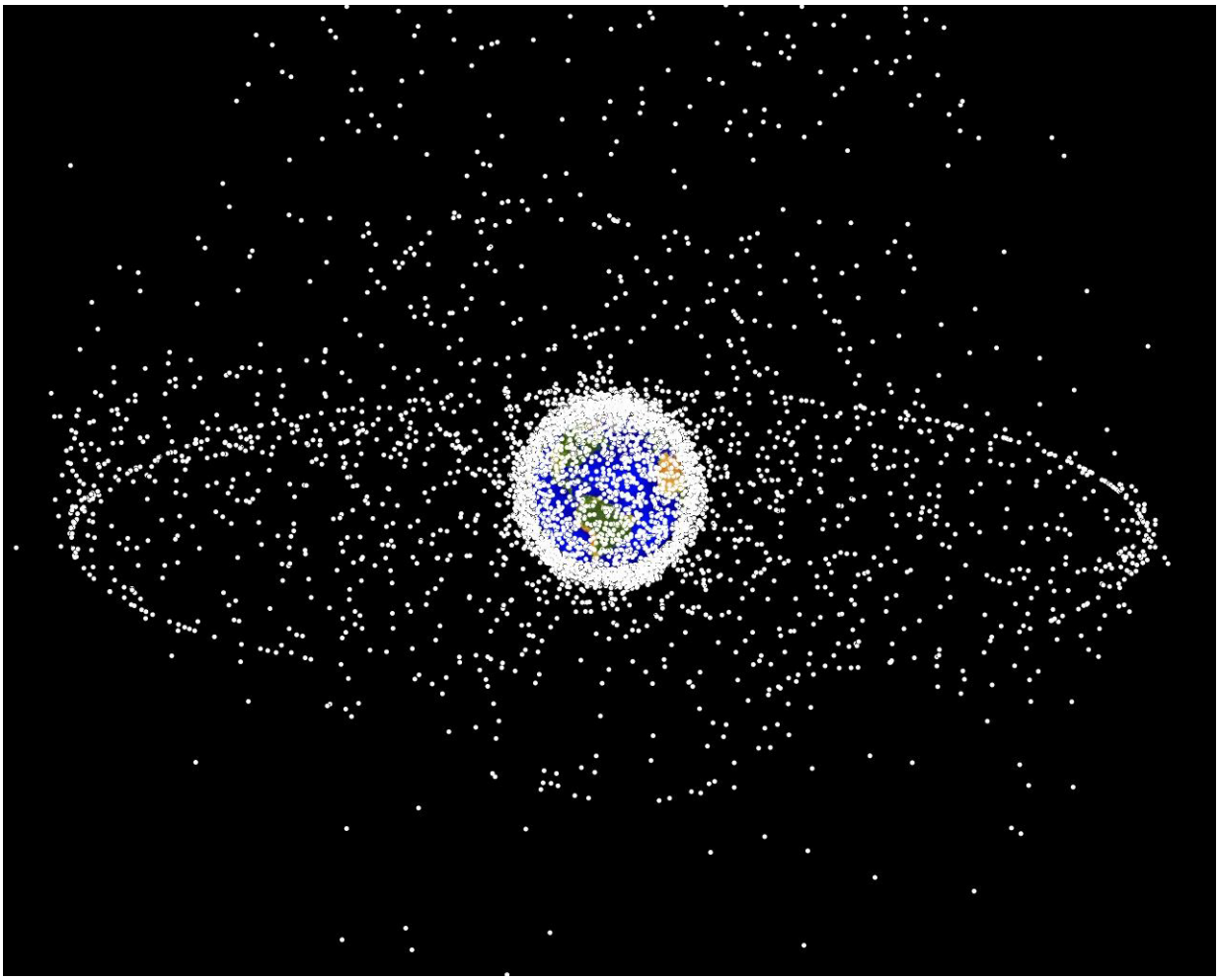

Figure 3. The GEO images are images generated from a distant oblique vantage point to provide a good view of the object population in the geosynchronous region. (Note: objects are not to scale) [19].

Thus, the *Space Surveillance Telescope* (SST), sponsored by the *Defense Advanced Research Projects Agency* (DARPA), was developed for the *Air Force Space Command* (AFSPC) to be fielded as a contributing sensor to the *Space Surveillance Network* (SSN) in 2011 [12]. The SST is a Mersenne-Schmidt telescope with improved capability over the legacy system like the *Ground-Based Electro-Optical Deep Space Surveillance System* (GEODDS) based on Ritchey-Chretien design [20]. The SST was originally developed to fulfill an existing gap in the SSN by overcoming and augmenting the limitation of the legacy system in detecting and tracking a small space object in GEO and Deep Space [12, 21]. As intended, the SST's 3.5

meter diameter spherical primary mirror with a 3x2 (6) degree wide *Field-Of-View* (FOV) gives a significant performance improvement over the GEODDS's one meter primary mirror with a 1.68 degree FOV [20, 22]. The SST's larger mirror enables improved detection capability and wider FOV for scanning of the night sky at a faster rate.

The uniqueness of the SST is its spherical primary mirror with a curved focal surface and a spherical correcting lens, known as a Schmidt corrector plate which is located at the center of curvature of the primary mirror with a diameter of 3.5 m as shown in Figure 4. The detector is placed at the prime focus and this design allows very fast focal ratios, while controlling coma and astigmatism [22]. However, because the Schmidt cameras have curved focal surface, a detector is correspondingly curved. Uniqueness of the telescope design enable longer tube length, however there are drawbacks, including obstruction of light and loss in contrast of images due to diffraction effects [22]. Additionally, because SST uses three large lens, effects of the aberration is even greater. Aberrations in the optical system cause further phase error which will be discussed in Section 2.2.1.

The SST program office modeled the telescope's wavefront error using the Zernike polynomials. This technique is one of the key processes that help to improve the SST's detection capability. By using estimates of the Zerknike polynomial coefficients produced by phase retrieval, it enables the SST to better achieve focus and alignment, which ultimately improves the *Signal-to-Noise Ratio* (SNR) and detection performance [22].

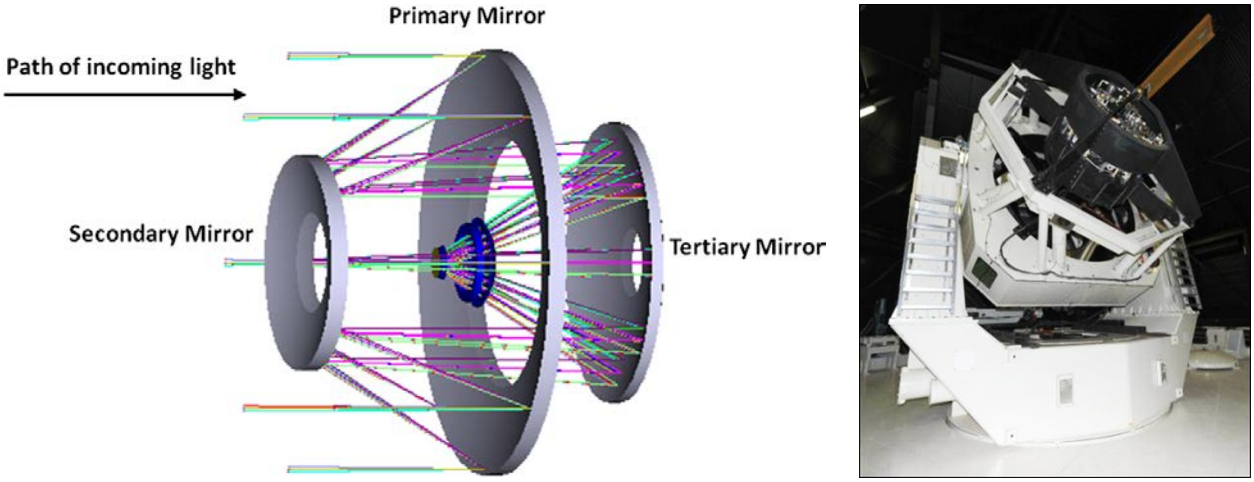

(A) (B)

Figure 4. (A) Optical layout of the SST. Light enters the system from the left in this image [22]. (B) Image of the SST system [12].

1.2 Problem Statement

Although the SST provides greater capability than the existing legacy systems, there is still a gap in the global coverage of the GEO belt as shown in Figure 5. Currently, with one SST located in Socorro, New Mexico, and three existing GEODDS located in Maui; Hawaii, Socorro, New Mexico; and *Diego Garcia* (DGC), Indian Ocean, there are coverage gaps in the Western Pacific and Atlantic region. With re-balancing of U.S interest from the Middle East to East Asia, also known as "Pivot to Asia," SSA of the Western Pacific region became even more crucial in pursuing the U.S National Space Policy [23, 24].

In order to prove the capability to achieve a global coverage, DARPA is planning to relocate the SST from its current mountaintop location in Socorro, New Mexico, United States to Exmouth, Australia in 2016. Relocating and providing its operational capability in a harsh observing environment will provide a crucial SSA coverage of the Asia Pacific region [21, 25].

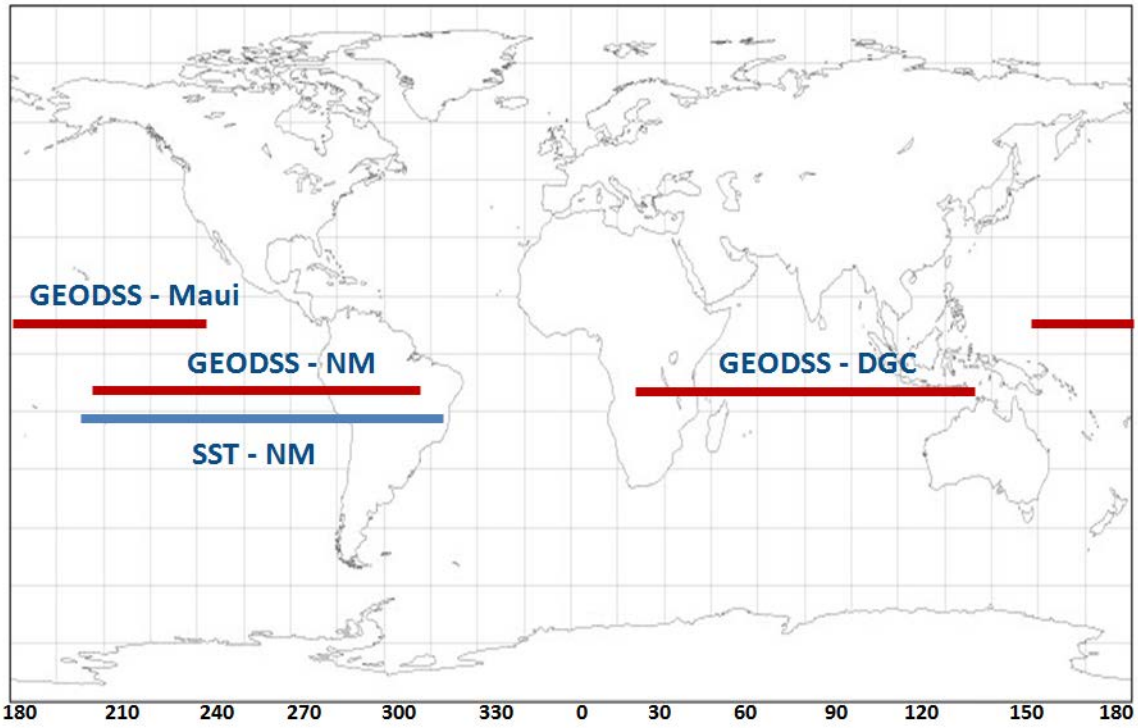

Figure 5. Current Ground Optical Coverage with three GEODDS and one SST. Three GEODSSs are located in Maui, HI, Socorro, NM, and Diego Garcia, Indian Ocean. The SST is located in Socorro, NM. [25].

However, the performance of the SST in Exmouth, Australia cannot be determined without conducting *Modeling and Simulation* (M&S) exercises using the *Point Spread Function* (PSF) of the SST. When compared to Socorro, New Mexico, Exmouth, Australia has much less favorable seeing conditions. It is estimated that Socorro has a seeing parameter of 8cm versus Exmouth's, of 5cm, which will be discussed further in Section 2.2. According to the M&S performed via MATLAB, the performance of the SST will most likely be degraded significantly with the use of current detection algorithms as illustrated in Figure 6.

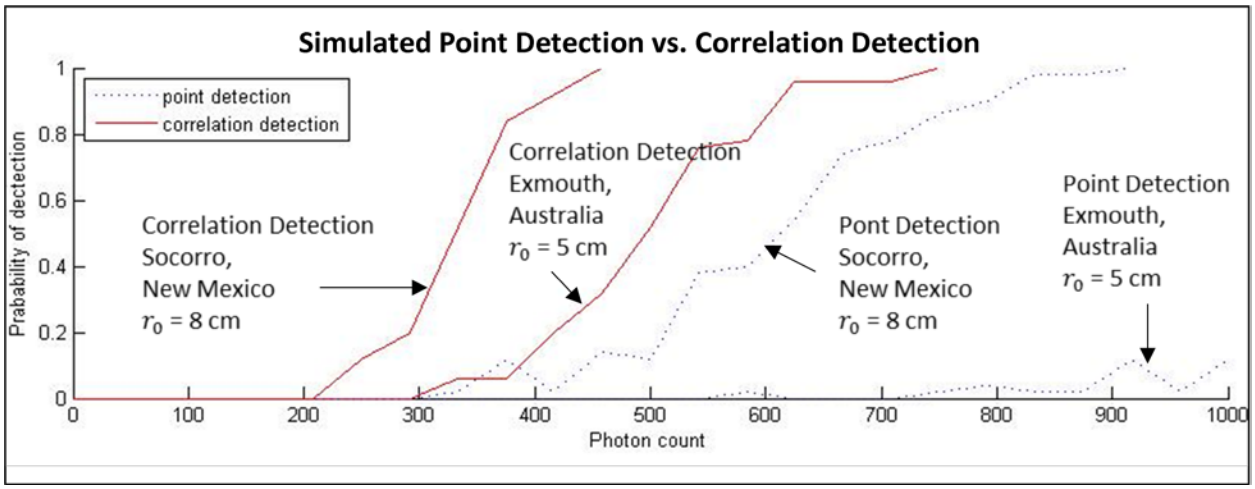

Figure 6. Simulated point detection versus correlation detection algorithm with seeing parameter of 5cm and 8cm, showing a significant increase in SNR is need for the same probability of detection.

In order to provide global coverage, the program office, which consists of the Air Force Life Cycle Management Center, *Space and Missile Center* (SMC), and DARPA, is seeking an option to acquire additional ground based optical systems, which might include other SSTs, or a hybrid of the GEODSS and SST. The SMC proposed placing new optics in the Mediterranean region and back at Socorro, New Mexico. In addition, SMC recommends augmenting the upgraded *Air Force Optical and Supercomputing* (AMOS) 1.2 meter telescope to fill the coverage gap and to provide overlapping coverage of the Pacific region, which would provide a maximum GEO belt coverage as shown in Figure 7 [25].

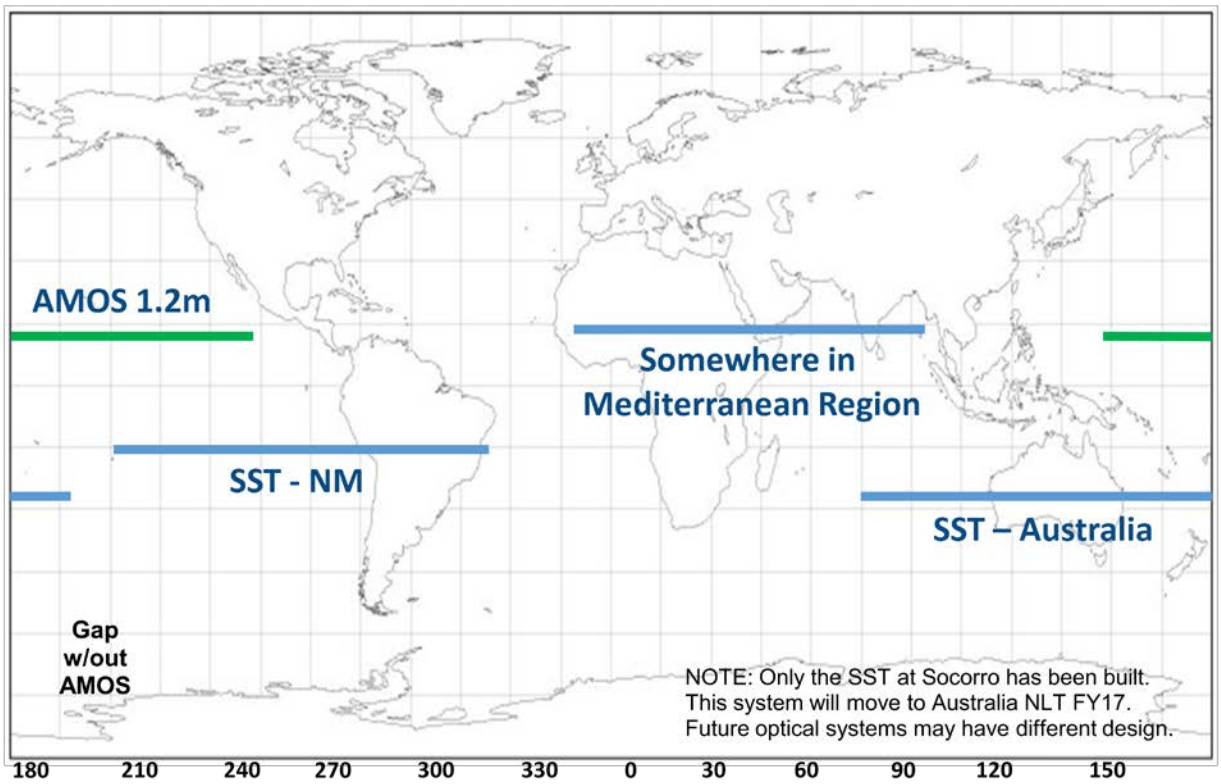

Figure 7. Three Site SST + 1.2m AMOS Upgrade. Next generation optics is proposed to be placed in Exmouth, Australia, Mediterranean Region, and Socorro, New Mexico. Upgraded AMOS is proposed to be placed in Maui, Hawaii to fill coverage gap and provide overlapping coverage [25].

1.3 Research Goals

The goal of this research effort is to improve the performance of the SST with the introduction of a new detection algorithm and to simulate the performance of the SST in Exmouth, Australia when the system utilizes existing and new detection techniques. A new detection algorithm, a MHT_6, based on the *Maximum Likelihood Test* (MLT) will be implemented to produce a probability of detection. But, in order to implement, test, and compare the performance of the detection algorithms, a new method of obtaining the true atmospheric seeing parameter, determining the initial point, and parameters to be used for an accurate comparison will be investigated. This research is one part of an overall effort to improve the

performance of the SST to strengthen SSN and overarching *Space Domain Awareness* (SDA) mission, which is an ongoing effort currently undertaken by DARPA and DoD.

1.4 Literature Review

This section examines previous research done in the field of remote sensing, specifically dealing with an image processing techniques to improve the performance of GBOs. The purpose of this literary review is to provide background information required to understand different methods available, that improves the detection of space/orbiting objects. There have been numerous research efforts carried out in the areas of image processing techniques, but in this literature review the SST system model and three specific detection techniques will be discussed. The three detection techniques are point detection, correlation detection, and the MHT_{10} detection technique.

1.4.1 Lincoln Near Earth Asteroid Research (LINEAR)

With the collaboration between the *Massachusetts Institute of Technology Lincoln Lab* (MIT/LL), United States Air Force and NASA, the *Lincoln Near Earth Asteroid Research* (LINEAR) detection algorithm originally was developed to achieve a high rate of search, processing, and discovery [26, 27]. The LINEAR process improved the NEO detection as mandated by Congress and the promising results from the LINEAR mission eventually lead to adaptation and implementation of its system model onto the SST's detection algorithm [19, 20]. The LINEAR detection algorithm has five major steps as shown in Figure 8.

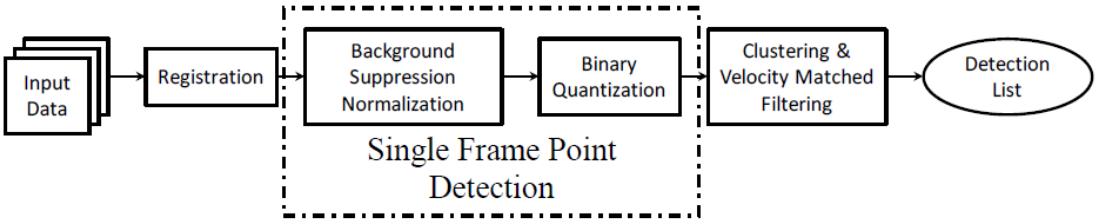

Figure 8. Block diagram of LINEAR system used to acquire asteroid data and detection algorithm [26].

First, the input data consists of three to five *Charged-Couple Device* (CCD) images of the same location of the sky collected by a user defined interval [26]. Second, image registration is performed to correct any errors by shifting through all frames except the first in order to line up their stellar backgrounds with that of the reference image [26, 28]. Third, the single frame point detection is a two step process, which includes the background suppression normalization and binary quantization. In the background suppression normalization, registered images are normalized to equalize the amount of noise in the clutter suppression normalization block. Then the normalized data are then binary quantized with a given threshold [26, 28]. Fourth, data are clustered on a frame-by-frame basis to group adjacent pixels into objects. Then the algorithm calculates and determines the centroids and extents of the clusters. The velocity matched filter then filters any objects that do not meet the desired rates of motion of interest(s) [26, 28]. Finally fifth, detected objects are cataloged and matched with a database of the orbital objects.

1.4.2 Point Detection

The point detection method is the baseline detection algorithm currently employed by the SST. It is based on the LINEAR process of the background suppression normalization and binary quantization process as discussed in Section 1.4.1. This process detects an object in

sample data by checking a single CCD pixel at a time. In this process, SNR is mathematically represented as Eq. (1) [28]:

(1)

where $d(c_x,c_y)$ is the SST imagery data with coordinates (c_x,c_y), is the standard deviation of the noise, is the detection threshold, and is the local background. If the pixel has a SNR greater than the threshold value , then it'll be classified as containing a target and passed on for further processing. If the pixel has a SNR less than the threshold, then it is classified as an empty pixel and no further action will be taken [29]. The SST currently uses a threshold value of 6 for .

Because the SST's PSF is much larger than the size of a single pixel, the SST data is binned into 2 by 2 pixels. As a result, there are two fundamental weaknesses and limitations of the point detection current algorithm used by the SST. First, binning makes position of the object a problem. If the object is not in the center pixel, binning magnifies the position uncertainty of an object and PSF shape. This results in the SNR becoming highly variable. Second, if an object is not centered on a single binned pixel, the SNR is greatly reduced [28].

1.4.3 Correlation Detection

The correlator is designed to achieve a chosen probability of false alarm when object is not present. Here, the image noise can be modeled as a Gaussian, which matches the SST's readout noise distribution. However, use of a Poisson distribution would also be equally valid,

but calculation in [30], revealed that using a flat background and an approximation of the threshold yields same calculation as the correlation detection using a Gaussian distribution [30].

The correlator SNR is represented by Eq. (2), where the threshold is expressed in terms of the SNR [28].

$$\frac{\qquad}{\qquad} \tag{2}$$

In single frame detection, a correlation detector performs better than the point detectors. However, according to [31], the author demonstrated the effects of the undersampling can have on the performance of the correlation detectors.

The point detection process used by the LINEAR has two key limitations due to undersampling. First, the Rayleigh sampling with cross-correlation performs poorly when the object fall in the corner of a pixel. This can be attributed to the fact that the Rayleigh pixel size is 2.44 times bigger than the Nyquist pixel. Due to larger pixel size, when an object is moved from the center pixel to the corner pixel, the shape of PSF changes. This causes the cross-correlation to yield low values, which results in the probability of detection to suffer [31].

Second, unlike the Nyquist sampling, in the Rayleigh case if an object does not fall in the center of the pixel, performance drops significantly as shown in Figure 9 [32].

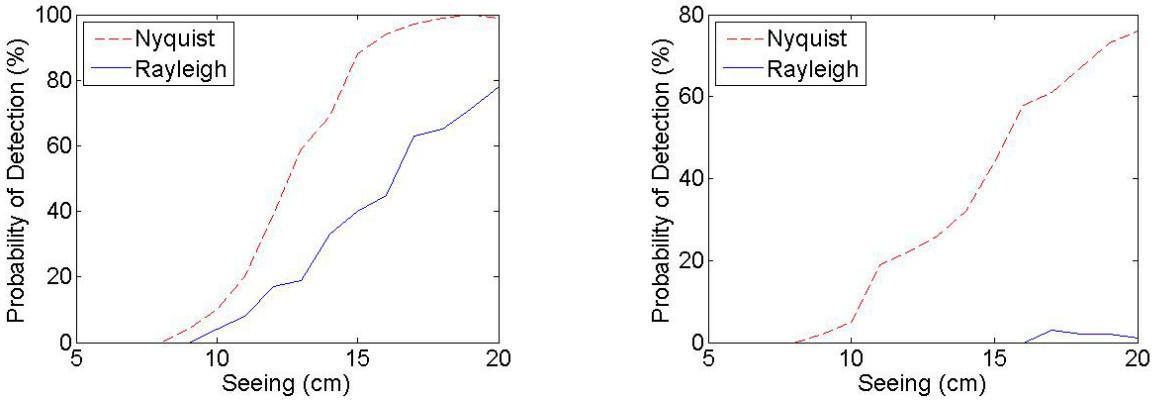

Figure 9. Comparison of aliased and unaliased detector performance for a fixed probability of false alarm (A) Nyquist and Rayleigh sampled correlator detection performance with PSF centered on a pixel (B) Nyquist and Rayleigh correlator detection performance with PSF centered on the corner of a pixel [32].

In conclusion, the performance of the correlation detection algorithm developed for the Panoramic Survey Telescope & Rapid Response System (Pan-STARRS) is an improvement over the baseline detector currently used by the SST. However, the performance of the SST is limited by the undersampled data.

1.4.4 Multi-Hypothesis Testing Detection

A MHT detection method is an improvement over the correlation detection method because it addresses two weaknesses of the correlation detection technique. The first is that the image of an object does not always fall in the center of the pixel. Second, is that a simple correlation operation does not always describe the shape of the sampled PSF depending on where the object is imaged on the array. The MHT allows for the possibility that the image is in different places within the detector. In [28], the author uses the strategy of using the MHT_{10}, , where is that an image of a space object is not present in the pixel, and the

nine different sampled PSF shapes correspond to the presence of a space object in nine different sub-pixel locations as shown in Figure 10. [28].

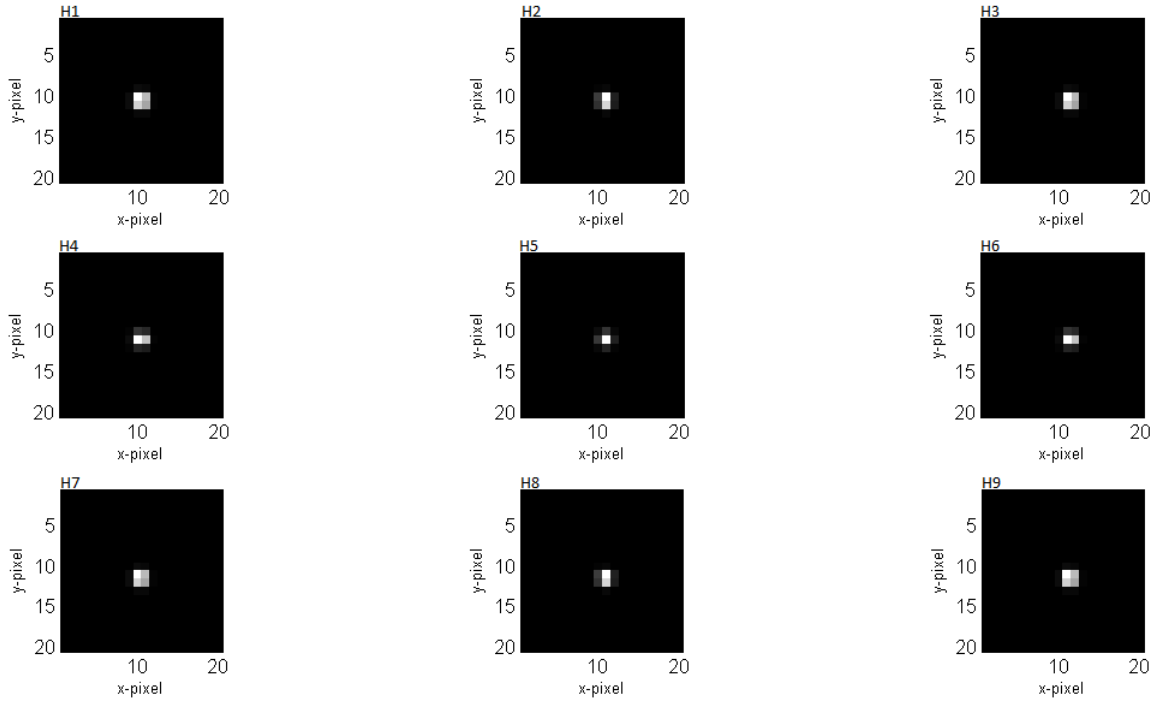

Figure 10. The hypothesis that the PSF is in the either the center of the pixel, , on the sides, , or corner of a pixel, .

The mathematical expression for the MHT is derived in [28] and is similar to the correlation detection test, except that the MHT tests out nine different possibilities, or hypotheses plus the image not being present in the pixel as defined by Eq. (3) [28].

(3)

Where are alternative hypothesis sub-pixel shifted PSFs, is M-ary detection threshold, is hypothesis that no object is present and is the hypothesis that an object is present as shown in Table 1.

Table 1. Alternative Hypothesis Sub-pixel Shifts for M=10. represents center pixel, represents side pixels, and represents corner pixels [28].

Alternative (i)	Horizontal Shift	Vertical Shift
1	-15	15
2	-15	0
3	-15	-15
4	0	15
5	0	0
6	0	-15
7	15	15
8	15	0
9	15	-15

But, because all nine hypotheses get tested in the MHT, the chance of false alarm occurrences increases as well. To ensure the MHT does not raise the probability of false alarm, , over the existing BHT used by the SST, an upper bound on the is calculated and then that upper bound is used as an estimate of the false alarm probability. To find the upper bounds of the , two assumptions are be made. First, that all tests are mutually exclusive and statistically independent. Under these assumptions, the numerical computation reveals that the estimated for the MHT is higher than the BHT. This problem can be eliminated by increasing the value of so that the of the MHT matches that of the BHT.

Simulations using the measured data of the ANIK-F1 reveal that the MHT always outperforms the point and correlation test as shown in Figure 11.

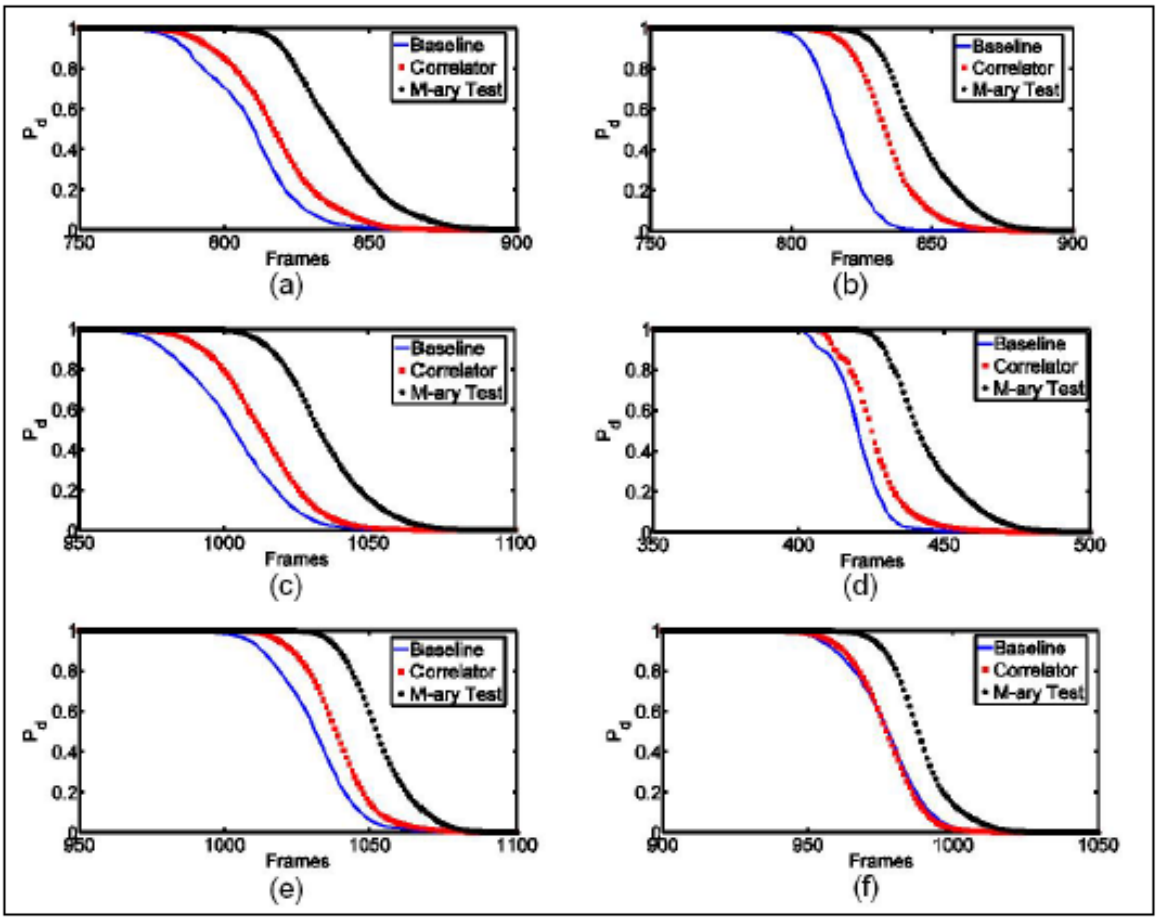

Figure 11. Comparison of the baseline detector, the correlator, and M-ary test probability of detecting ANIK-F1 as it enters eclipse on (a) 13 Mar 2012 (b) 14 Mar 2012 (c) 15 Mar 2012 (d) 21 Mar 2012 (e) 22 Mar 2012 (f) 23 Mar 2012, where the is equal for all three detectors [28].

Therefore, when an object is not centered on a single pixel, the MHT significantly improves the detection capabilities of the SST compared to the BHT. It's important to note that the SST's focus is detection; therefore it's unlikely that any object will repeatedly fall in the center of a pixel during the three consecutive frames used for detection.

In addition, the author proposed data normalization using outlier rejection technique, which can be used to improve the detection performance of MHT. This feature is designed to compute the background noise statistics using a reduced set of data from the window around the pixel to be tested. This noise power estimation technique rejects any noise sample in the window

surround the pixel to be tested, whose values do not conform to those predicted by Gaussian statistics [28]. By doing so, when computing for the noise generated by the background light, bad pixels, noise spikes, and nearby stars are not incorporated into the computation.

The gains in the detection performance by the MHT are realized by mitigating the aliasing effects of undersampling using a phase retrieved PSF model. Additionally, the MHT also provides sub-pixel position information and more accurate estimates of object irradiance. However, the down side is that it requires six times more computing processing power [28].

Although analysis and performance of ten hypotheses is described in detail in [28], the author does not investigate the performance of the MHT using different number of hypothesis. This research will investigate the performance of the MHT_6 and results will be compared against MHT_{10} used in [28].

1.5 Implications

The results from this research effort could be used to predict the performance of the SST in other candidate sites. An improved detection algorithm found from this research can be applied directly to the current operations at the SST, other optical system such as GEODDSs and Pan-STARRS (currently being implemented), and next generation SBOs. Application of the new detection algorithm can improve the performance of the legacy systems with little or no cost to the Government, depending on availability of computer equipments and network.

Furthermore, if applied to the GBOs with the NEO mission, it could be a part of contribution in an overall effort to meet the Congressional mandate to have 90% of all NEOs over 140 meters in diameter catalogued by 2020 as stated in the NASA Authorization Act of 2005 [7]. Any such

notable improvement would enhance the SSA and SDA capability, which will ultimately help support the U.S. National Space Policy.

1.6 Thesis Organization

In this thesis, *Chapter II* describes the system model of the SST and AFIT telescope, the atmospheric model, and the MHT algorithm using number of hypotheses. *Chapter III* details the experimental set-up, data collection, and processing method. *Chapter IV* provides an in-depth analysis of the results of the experiments. Lastly, *Chapter V* gives a summary of the research, provides conclusions on the thesis, and offers recommendations to expand this effort for future work.

II. Methodology

When the light from the point source propagates through the atmosphere and optical system, its shape gets distorted by the atmospheric turbulence and optical aberrations. This resulting distorted image of the point source is the PSF. Therefore, it's crucial to understand the characteristics of the entire system in order to get accurate results. The image formation can be modeled as a linear process and broken down into the atmospheric model and optical system model.

The purpose of characterizing the AFIT telescope model is to provide an additional set of measured data, which could be used to strengthen the fidelity of analytical model for calculating the . In addition, the AFIT telescope will test the performance of the detection algorithms observing non-static space object with much different value then at Socorro, New Mexico or Exmouth, Australia, which will be discussed in Section 4.2.

Although the SST and AFIT telescopes have different system parameters, the unique system specification of the AFIT telescope allows it to become a scaled down version of the SST system with scaled value, which will be discussed in Section 3.2.

The system parameters of the SST and AFIT telescope system is listed in Table 2.

Table 2. The SST and AFIT telescope system parameters [29].

Parameter	SST	AFIT telescope
CCD Pixel Size	30 m x 30 m	16 m x 16 m
Primary Mirror	3.5 m	.2 m
Focal Length	3.5 m	2 m
Center Wavelength	500 nm	533 nm

2.1 Optical System Model

The optical system model must be understood and characterized in order to determine the effects it has on the total phase and PSF. Two optical models that will be characterized in this research are the SST system model and the AFIT telescope model.

When optical telescopes such as the SST and AFIT telescope view objects that are very distant, those objects effectively become a point source to the telescope. When using geometric optics, the ratio of the pixel size approximation to the focal length is comparable to the size of the object over the distance from the telescope, which makes all potential objects appear as point sources.

2.1.1 SST System Model

The PSF of the SST optical system, can be represented as Eq. (4) [33]:

(4)

where are pixel coordinates in the detector plane, are pixel coordinates in the pupil plane, is a pupil function that describes the effect of the pupil on incoming light, and is a two-dimensional Fourier transform. Although the SST has support arms and secondary mirror obstruction, these support arms are not modeled in the system due to their negligible impact on the production of the final image. However, SST does not have a perfect lens or mirror, so aberrations of the lens must be accounted for in the SST model. In every curved lens, there exist inherent flaws known as aberrations because in practicality, no lens can be perfect. Aberrations are anomalies that cause light to be improperly focused. Aberrations can result in light not constructively interfering at the focal point, that are caused by a mismatch between the

propagation phase and the lens transformation; as well as imperfections in the lens and mirror surfaces [22]. Imperfection in the lens or mirror causes phase distortions and these distortions are modeled as the phase fluctuations to the amplitude function as represented in Eq. (5) [33].

(5)

where is an amplitude function that is one or zero, depending on if light passes through the pupil at the pixel location. The phase aberrations are expressed as the sum of a set of orthonormal Zernike polynomials, with each polynomial representing a type of aberration or phase distortion as represented in Eq. (6) [34].

(6)

The residual error coefficients, represent the amount of the Zernike polynomial present in the optics and these coefficients are unique to the optical imaging system. Aberration present in the optical telescope system must be experimentally measured in order to create an accurate model of the optical PSF. Finding values of these coefficients for a three mirror optical system like the SST can be very difficult, but a method for obtaining the Zernike coefficient values can be found in [22]. Here, the author discovered a technique to experimentally measure first eleven coefficients of SST's optics. The value of the coefficients can change over time, but the values obtained from [22] are used to simulate the aberrations of the SST system. Although there are potentially hundreds of Zernike coefficients, only the first eleven coefficients are used in modeling for two reasons. First, the bulk of the power in the aberrations is contained in the lowest order polynomials. Second, because the SST system is

undersampled, any high frequency distortions will not be accounted for in the PSF, therefore higher order coefficients are unnecessary. Table 3, lists the measured coefficients for the first eleven polynomials of the SST system, and Figure 12, illustrates images of Zernike polynomials numbers .

Table 3. Measured optical aberration Zernike coefficients, for the SST.

Coefficient/Zernike Mode	Aberration	( ) / Value (Waves)
	Piston	2.087691892
	X-axis Tilt	-5.951781081
	Y-axis Tilt	-5.299943243
	Defocus	6.884924324
	45° Astigmatism	1.259810811
	90° Astigmatism	-0.278189189
	Y-axis Coma	0.275475676
	X-axis Coma	-0.727910811
	Y-axis Trefoil	0.354827027
	X-axis Trefoil	-0.481786486
	3rd order Spherical	-0.156713514

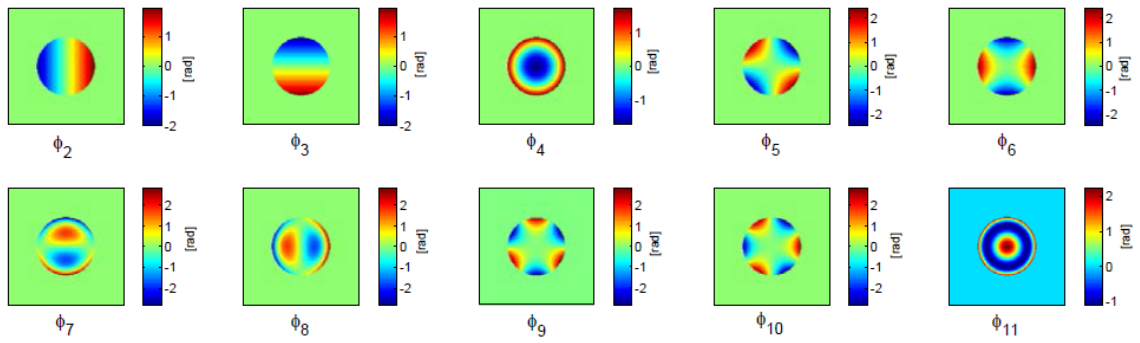

Figure 12. Images of Zernike polynomials numbers [29].

The Fourier Transform of the optical PSF can be multiplied with the long exposure *Optical Transfer Function* (OTF) founded in Eq. (17) in the frequency domain to obtain the combined OTF. Then the inverse Fourier is performed to obtain the new PSF model in spatial domain, as shown in Eq. (7) [29].

(7)

The model described in Eq. (7) would be correct if the image presented to the CCD detector is properly sampled. When the system samples the image at the Nyquist frequency, , the image is considered to be properly sampled because the Nyquist sampling theorem provides a prescription for the nominal sampling interval required to avoid aliasing or loss of signal. The Nyquist frequency is twice the cutoff frequency, of the system. The cutoff frequency, in an optical system can be represented as Eq. (8) [33]:

— (8)

where is the focal length of the system, is the center wavelength of the optical telescope, and is the diameter of the aperture. The necessary sample spacing can be found by using the inverse relationship between sampling frequency and sample spacing represented as Eq. (9) [33]:

— ——— (9)

The SST's required pixel spacing at the CCD that would avoid aliasing can be calculated by using Eq. (9), which is [29]. The SST's data collection involves pixels that are grouped in 2 by 2 data bins, yielding size of . Because , SST is not sampled at Nyquist. This means that a shift in where the image is formed in CCD can potentially cause different shaped PSFs as discussed in Section 1.4.3. To avoid this issue, shifting is performed prior to adjustment for the sampling and not after because [29] shows that the effects of shifting after the sampling does not adequately represent the effects of sub-

pixel motion. Two variables and are introduced to shift the PSF, . is to shift in the x-direction and is to shift in the y-direction as shown in Eq. (10).

(10)

Here, a circular shift can be utilized for the shift operation because the PSF is created in a large zero padded matrix, in order to avoid unwanted edge effects.

The pixel blurring function is then used to model the difference between the required and actual sampling with the assumption that the SST uses a square pixel CCD sensor. The blurring function can be expressed as rectangles in the x and y plane with a width of , where is the ratio of system sampling versus required Nyquist sampling, is more accurate PSF model because it represents the convolved and down sampling effects on the PSF of sampling at a frequency less than Nyquist.

(11)

where and are temporary convolution variables and and are the total number of pixels in the x and y direction respectively. The new PSF, is then normalized to sum to one, allowing the PSF to be scaled to match a specified object intensity as shown in Eq. (12) [29].

(12)

The final modeled PSF, is used in this paper.

2.1.2 AFIT Telescope Model

In order to replicate the SST system model, the process of characterizing the AFIT telescope model is nearly identical.

The PSF of the SST optical system, can be represented as Eq. (13).

(13)

The AFIT telescope also has a structure arm and other mirror obstructions, but these obstructions are not modeled in the system because their impact is negligible on the production of the final image. Although AFIT telescope does not have a prefect lens or mirror, due to difficulty of obtaining values for the residual error coefficients, the AFIT telescope will be modeled with having a perfect optic with no phase distortions as shown in Eq. (14).

(14)

As discussed in Section 2.2.1, the new PSF model, can be found by inverse Fourier Transforming the combined OTF, which is found by multiplying the Fourier Transform of the optical PSF with the long exposure OTF in the frequency domain, as shown in Eq. (15).

(15)

The new PSF, must be sampled in a way to match the SST sample spacing while meeting the Nyquist frequency requirement. First, by using Eq. (9), the required pixel spacing for the AFIT telescope is calculated.

As discussed in Section 2.1.1, the blurring function is then used to model the difference between required and actual sampling. is produced by convolving the optical PSF from Eq. (15) with Eq. (16),

(16)

The final modeled PSF, is used in this research.

2.2 Atmospheric Model

The atmosphere is one of the limiting parameters in determining the performance of a ground based optical system. Therefore, efforts in understanding, characterizing, and implementing the precise atmospheric models are essential in improving the performance of the given system.

There are two different atmospheric models that can be used to determine the effects of atmospheric turbulence on the total phase and PSF of the optical system. Two are the long and short exposure atmospheric model. The long exposure atmospheric model is used when the exposure time through the Earth's atmosphere is greater than 10ms [33]. Otherwise, if the exposure time is less than 10 ms, then the short exposure atmospheric model gets utilized. Because models have different effects on the total phase and PSF, an accurate atmospheric model must be applied during the phase retrieval process to determine the correct phase errors and PSF.

2.2.1 Atmospheric Effect

Atmospheric effects are one of the biggest challenges faced by the GBOs. For example, atmospheric effects cause a blurring of astronomical objects such as stars or in our case orbiting satellites caused by mixing of different layers of Earth's atmosphere. Each of the layers has a different optical refractive index because every layer of the atmosphere varies slightly in temperature, pressure, density, chemical composition, dust, and vapor content [35]. This causes light to refract slightly at different angles as it travels through different layers of the atmosphere as shown in Figure 13A. This effect results in image fluctuations such as blurring, scattering, shifting, and more [36]. The Earth's atmosphere acts like a random process to any light that propagates through it by perturbing the images of a point source as shown in Figure 13B.

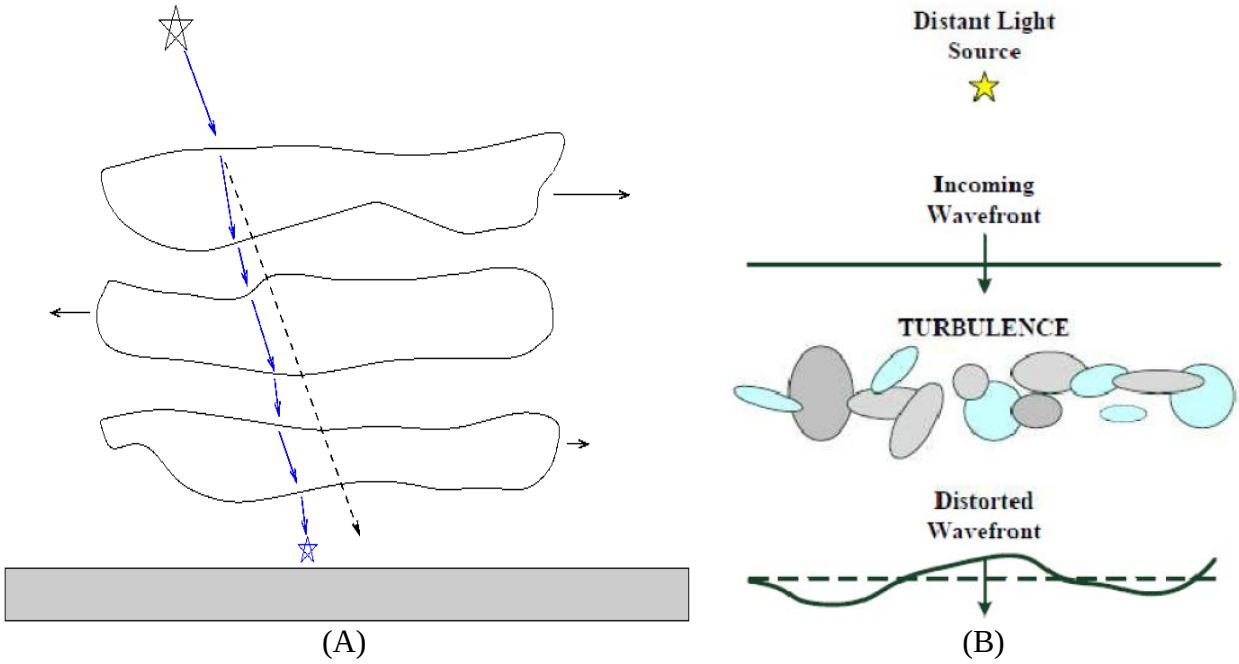

Figure 13. Atmospheric effect (A) effects of atmospheric layer on a ray [35] (B) effects of the Earth's atmosphere or turbulence on a plane wave [37].

This varying index of refraction determines the path averaged optical path length, where the difference in path lengths results in phase front distortions.

2.2.2 Atmospheric Seeing Parameter

The atmospheric seeing parameter or Fried parameter, , is the parameterization of the turbulence in the atmosphere [31]. It is a measure of the quality of optical seeing through the atmosphere due to the refractive index as discussed in Section 2.1.1. The blurring is caused by photons from the point source being spread over the wider pixel region of the CCD array instead falling into a single pixel.

The longer propagation pathway will result in greater phase front distortions. Therefore, higher elevation will provide better seeing because light has less atmosphere to travel through. Hence, in general it is more ideal to place the GBOs at a high elevation region for better performance.

The atmospheric seeing parameter is measured in centimeters and the linear dimension in units of centimeters represents the telescope diameter that would give maximum resolution allowed by the turbulence. The larger optics can collect more light which would increase the probability of detection, but cannot increase the resolution once the maximum resolution is reached. Due to the turbulence, the smaller optics collects less light which would decrease the probability of detection, but the resolution will not be affected as long as seeing parameter is less than the telescope diameter.

The atmospheric seeing diameter can be measured in two ways. The first is by simply using the seeing monitor pointed at the stellar object (i.e. stars) in the sky and measuring the movement of objects within the CCD array which would determine the atmospheric seeing parameter at that location [38]. The second method is by comparing the measured PSF against the simulated PSF. This technique can only work when the characteristics of the optical system are understood. Once the optical PSF is determined, utilizing the technique described in Eq.

(32), the simulated atmospheric turbulence can combine and resulting PSF can be compared against the measured PSF. Then the best fit model via *Mean Squared Error* (MSE) analysis would be used to determine the seeing diameter of the atmosphere, which will be discussed further in detail in Section 4.2.1. The second method will be used in Section 3.2, because there is no seeing monitor available.

2.2.3 Long Exposure Optical Transfer Function (OTF)

Although the atmospheric effect acts as a random process, through long integration times, T 100 milliseconds, the optical system can effectively average out the random atmosphere. Since the SST uses a shutter with an integration time greater than 25 milliseconds, the long exposure OTF, , derived in [39] can be used as an acceptable model. Therefore, in this research, the long exposure OTF will be used for both the SST and AFIT experiment and the short exposure OTF will not be utilized. The is the Fourier transform of the PSF, which represents the frequency response of the system to an impulse as shown in Eq. (17).

(17)

where and are spatial frequency variables at the image plane, is the focal length, and is the seeing parameter. A larger will have less effect on the optical telescope and vice versa for smaller .

2.2.4 Seeing Parameter versus Latitude

The current estimate of the seeing parameter at sites located in Socorro, New Mexico and Exmouth, Australia is based on measurements done by the MIT/LL. The method used by MIT/LL to measure the seeing parameter is by aiming the seeing monitor towards the stellar object as shown in Figure 14. This method predicates that the atmospheric path lengths will always be equal, regardless of longitude or latitude position as long as the elevation levels are equal.

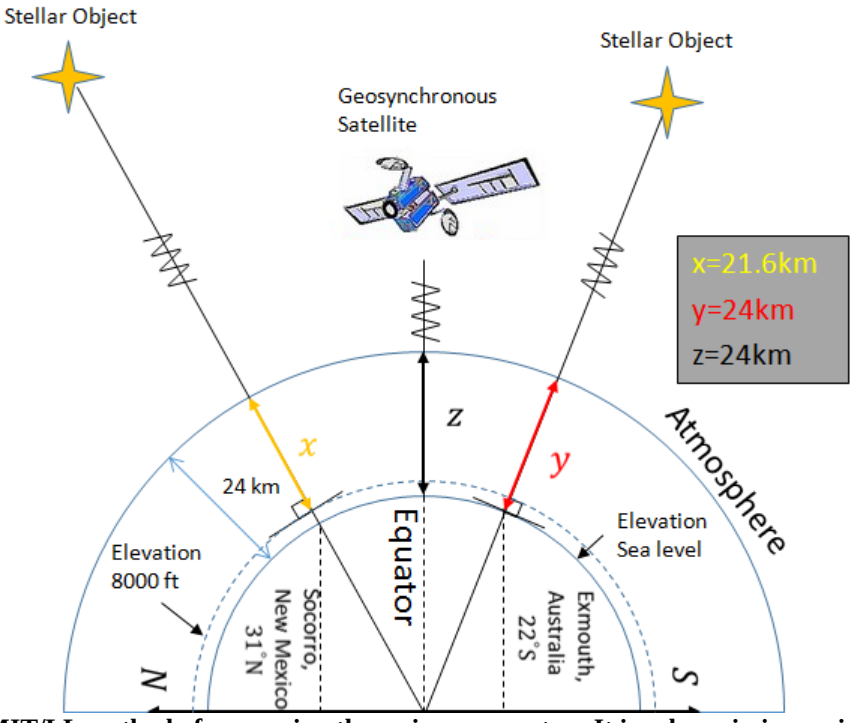

Figure 14. MIT/LL method of measuring the seeing parameter. It involves aiming seeing detector orthogonally to the viewing site. The path length X and Z illustrates that the atmospheric path lengths will always be equal, regardless of longitude or latitude position as long as the elevation levels are equal. (Note: objects are not to scale)

However, the issue arises when the goal is to observe objects that are not orthogonal to the viewing site because the SST's mission is to view objects in GEO. The atmospheric path length is one of the key parameters in determining the value. Hence, the utility of the method

used by the MIT/LL in measuring the is less accurate when used to model the SST's atmospheric model because a primary mission of the SST is to detect and track objects in a GEO belt.

If the goal is to observe object(s) in the GEO belt, the location of the viewing site in latitude becomes an important factor. As illustrated in Figure 15, the atmospheric path length changes depending on the latitude position of the viewing site. With elevation level being equal, the atmospheric path length increases as the distance from the equator increases. Therefore, the measured by MIT/LL will differ from the actual because the atmospheric path length from Socorro, New Mexico ( ) and Exmouth, Australia ( ) to GEO belt are greater than path length used by MIT/LL.

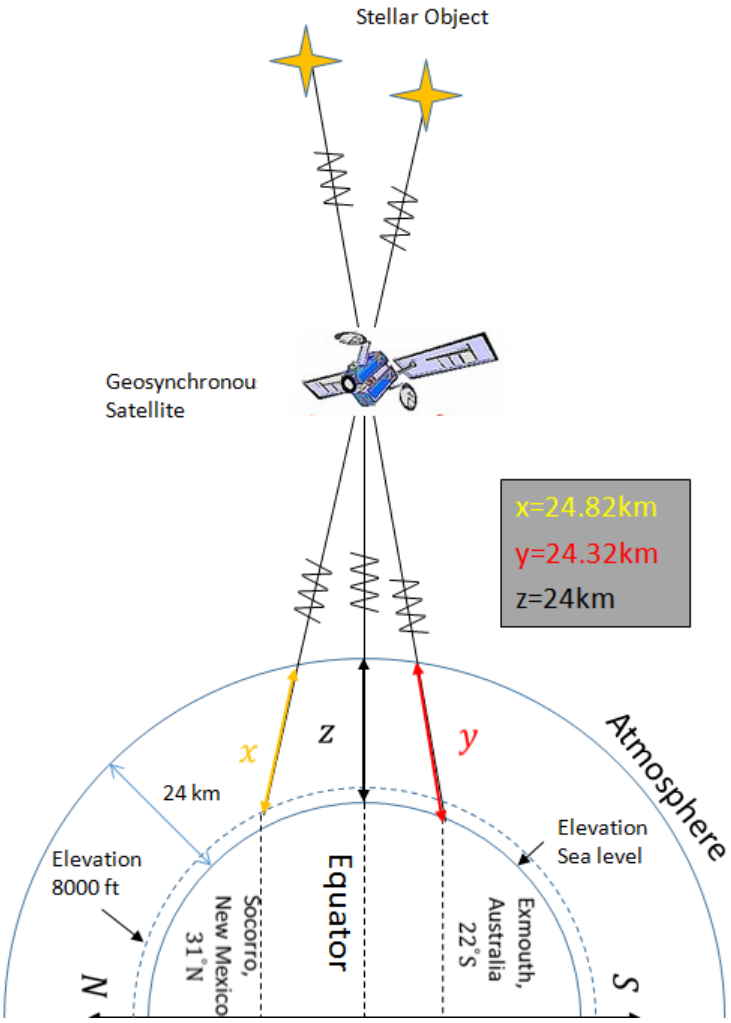

Figure 15. New method of measuring the seeing parameter. It involves aiming seeing detector towards GEO belt or stellar objects that's on the aligned path. The path length X, Y, and Z illustrates that the atmospheric path lengths depends on latitude and elevation. (Note: objects are not to scale)

This issue can be resolved by aiming the seeing detector towards stellar objects that aligns with the space objects located in GEO and obtain new values at Socorro, New Mexico and Exmouth, Australia sites. However, due to the availability of measured data, there aren't any data measurements with this new approach available. Therefore, true seeing parameters will be calculated numerically and compared against the analytical model obtained using via MATLAB in Section 4.4.

2.2.5 Seeing Parameter using Hufnagal Valley ( ) Profile

To find the value based on total path length, must be calculated first. This can be achieved using the *Hufnagal Valley* ( ) profile as shown in Eq. (42) [40]:

(18)

where is the wind speed and pseudo-wind based off the Bufton wind model, is elevation of viewing site, and is the nominal for a typical baseline or . It's important to note that to obtain an accurate result, will need to be calculated in an increment (one meter is used in this case) throughout entire atmospheric path length, . This method is utilized with the purpose of distributing atmospheric turbulence throughout entire atmospheric path length. Because atmospheric turbulence varies depending on altitude, the incremental approach allows appropriate values of turbulence being applied based on the altitude. If a uniform is applied, then atmospheric turbulence at that given altitude gets integrated thought the entire path length. This would result in much smaller at low altitude because atmospheric turbulence is stronger in lower altitude.

Now can be calculated using Eq. (19) [40]:3

(19)

where m=0 for plane wave. Using calculated , can be calculated using Eq. (20) [40]:

(20)

where m=0 for plane wave and .

The model described in Eq. (18) would be correct if the profile based on the is same as the one at Socorro, New Mexico and Exmouth, Australia. However, the true profile is unknown; therefore it must be either be measured or computed in order to validate the accuracy of the model. For this research, profile will be calculated numerically because it cannot be measured.

First the accuracy of the profile can be checked by comparing the calculated , using profile against the measured If results are equal, then the profile will be assumed to be correct for that location. However, if the results are different, then a new modified profile must be obtained. This can be accomplished by plotting versus .

Since the calculated in Eq. (18) is based on a path looking straight up, the angular path must be calculated. Angular atmospheric path length for both locations can be obtained from calculating the look down angle, , from the commercial GEO satellites to viewing locations as illustrated in Figure 16.

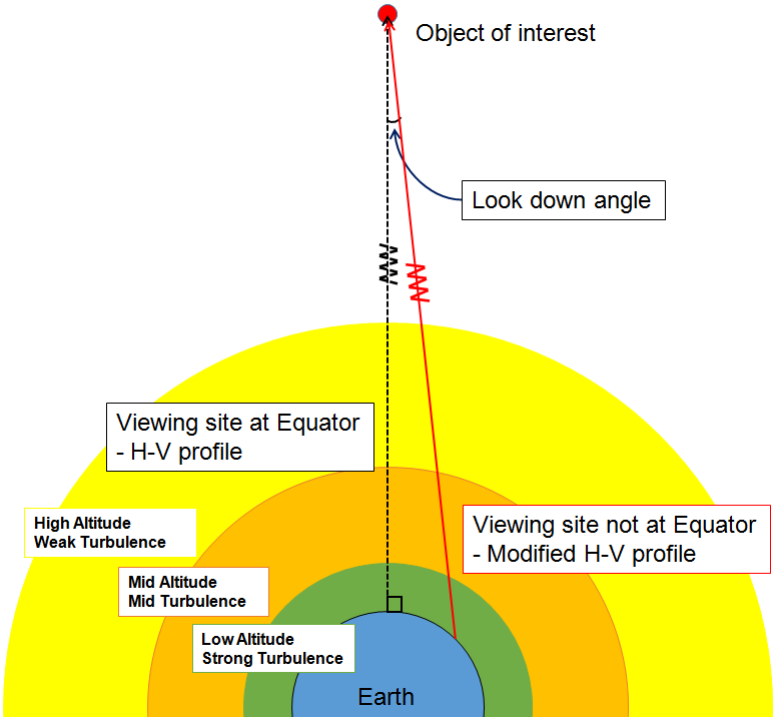

Figure 16. Geometry for calculating the . (Note: objects are not to scale)

This is made possible by the fact that the commercial television satellites and viewing sites are on same longitude. The look down angel for Socorro, New Mexico is 39.6 degrees and Exmouth, Australia is 25.7 degrees [41]. Using angular path length, angular and can be obtained by using Eq. (44, 45).

(21)

(22)

2.3 Multi-hypothesis Test (MHT) Algorithm

As discussed in Section 1.4.4, the MHT is an improvement over the BHT because in a MHT, M different numbers of hypotheses are considered instead of just the two. In the case of

the BHT, when only two hypotheses are considered (object being present or not present) the object's sub-pixel shifts on the CCD array will not only change the object's position, but also the shape of the resulting image due to aliasing as discussed in Section 2.1.1. But in the MHT, each hypothesis corresponds to a particular set of input conditions where each input condition represents a modeled PSF viewed through an optical system. The MHT utilizes these additional PSF distributions to achieve a higher probability of detection.

The spatial shifts in the and plane are determined by variables and , and the model for objects located in the center, sides, and of a corner pixel. The number of hypotheses and their position location determines the performance with tradeoffs. In this research, for the MHT a strategy of using six hypotheses, will be investigated, where being that an image of a space object is not present in the pixel, plus the five different sampled PSF shapes as shown in Figure 17. An alternative hypothesis with the sub-pixel shifts are listed in Table 4.

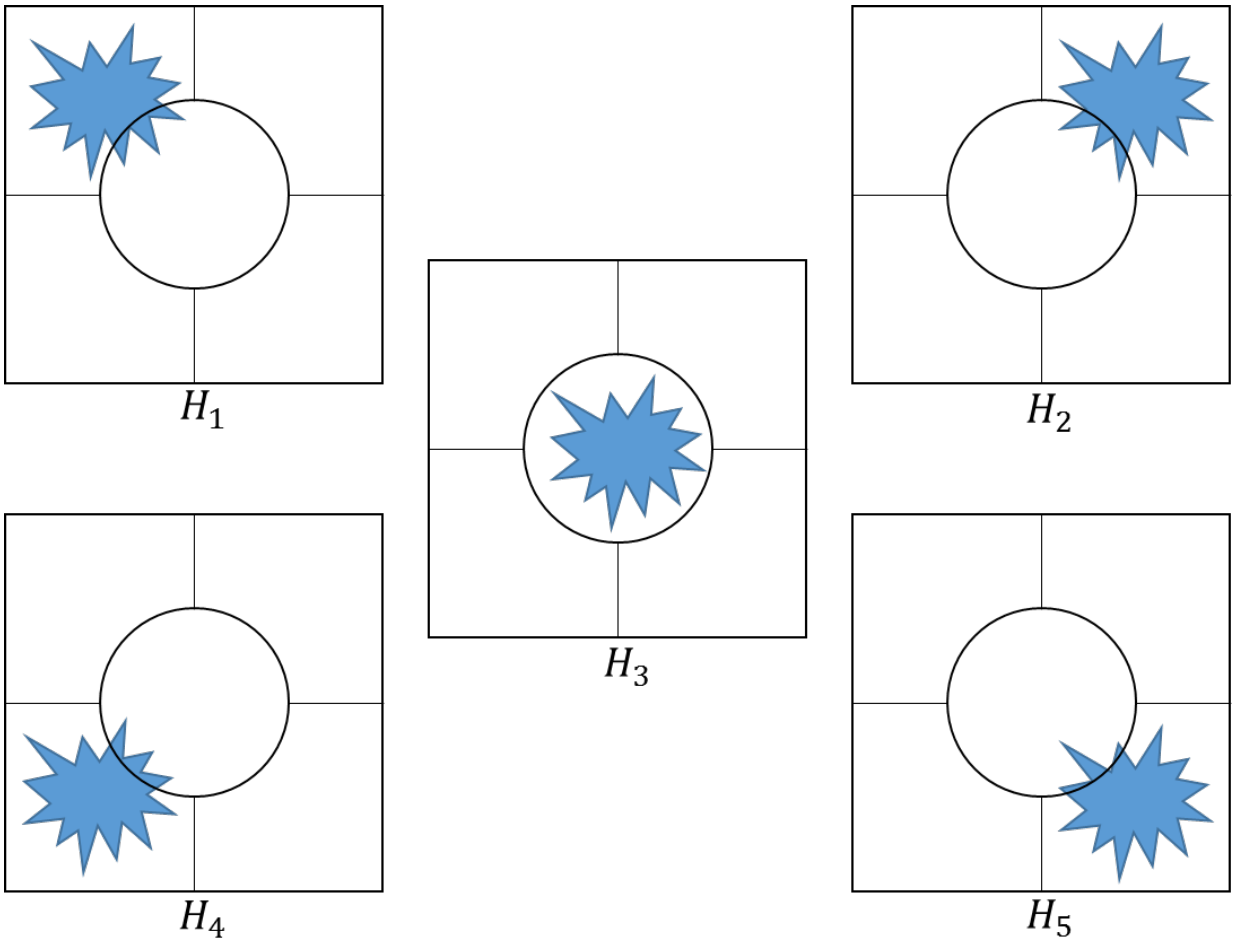

Figure 17. The hypothesis that the PSF is in the either in the top left of the pixel , top right of the pixel , center of the pixel, , bottom left of the pixel , or bottom right of the pixel .

Table 4. Alternative Hypothesis Sub-pixel Shifts for M=6. represents top left corner pixel, represents top right corner pixel, represents center pixel, represents bottom left corner pixel, and represents bottom right corner pixel.

Alternative (i)	Horizontal Shift	Vertical Shift
1	-15	15
2	15	15
3	0	0
4	-15	-15
5	15	-15

The SNR of an individual pixel can be determined via the Likelihood Ratio Test (LRT). In the BHT, when the object is located in the side or corner pixel instead of center, the peak intensity of the center pixel decreases. The spread of photons to adjacent pixels in turn decreases

the SNR value of the pixel being tested, which causes the probability of detection to suffer. A correlation algorithm is implemented to mitigate this effect because correlation compares the entire expected PSF instead of just a single pixel [42]. This technique can be applied to the MHT with multiple hypotheses as well [29]. An example of the division of a pixel into sub-pixel locations for varying M is illustrated in Figure 18.

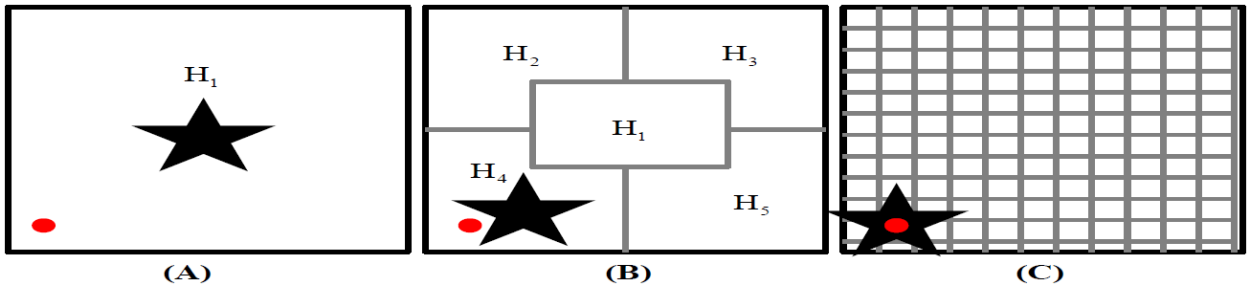

Figure 18. An example of the division of a pixel into sub-pixel locations for varying M. (A) BHT with M=2 (B) MHT with M=6 (C) MTH with M=122.

The circle dot indicates the true location of the object and the lines indicate the separation of the sub-pixels in its decision areas. Figure 18A, illustrates a simple BHT with two hypotheses, where the object is assumed to be at the center of the pixel. However, if the object falls outside of the center pixel, in this case bottom left corner, performance of both the point detector and correlation BHT suffers. This is due to the inability of both detectors to adequately capture the resulting PSF, which yields a low probability of detection. Figure 18B, illustrates a MHT_6 where sub-pixel hypotheses are at the center and four corners of the pixel. In this scenario, a probability of detection would increase. This is due to the corner pixels ability to capture and create a modeled PSF, which allows stronger correlation between the modeled and observed PSF. Figure 18C, illustrates a highly dense MHT with 121 hypotheses which is similar to Figure. 18B. In this scenario, the modeled PSF will correlate well with the observed PSF. With the small shifts in sub-pixel locations used in Figure 18B and Figure 18C, there will not be

noticeable improvement in the performance of the probability of detection because noticeable changes in the PSF will not occur.

Although, increasing the number of hypotheses, M, from two to six and more has some benefits, it also has drawbacks. The two main drawbacks are the probability of false alarm and computational cost. First, additional hypotheses introduce error to the decision criteria because a large number of the alternative hypotheses may have a higher chance of resembling random noise present in the system. This causes the false alarm rate to increase. Second, the creation and testing of additional hypotheses increases the computational cost which can be an issue if a real time data processing is required. Therefore, a trade-off between the number of hypotheses versus the detection capability and computational cost must be understood.

2.4 Summary

This chapter described the methodology for characterizing and modeling an optical system and atmosphere, as well as theory supporting algorithm using MHT_6. The methodology for characterizing the optical system addressed the SST system model and AFIT telescope model, and the atmospheric model addressed the effects of the atmosphere and importance of the seeing parameter. Furthermore, the relationship between the latitude position and atmospheric path length was investigated. Lastly, the theory behind the algorithm using MHT_6, as well as comparison against the BHT and MHT using 122 hypotheses was discussed. Experiments using these methods will be conducted in the next chapter.

III. Experiment

In this research, two experiments were conducted. The SST experiment was conducted to determine which type of detection algorithm is best at detecting dim, unresolvable space objects. The AFIT telescope experiment was conducted to collect data and compare the results against the analytical model for calculating . There are two purposes of characterizing the AFIT telescope model. First, is to provide an additional set of measured data which could be used to strengthen the fidelity of the analytical model for calculating . Second, is to provide performance result of the detection algorithms observing non-static space object, with much different then in Socorro, New Mexico or Exmouth, Australia. Although the SST and AFIT telescopes have different system parameters, the unique system specification of the AFIT telescope allows it to become a scaled down version of the SST system. In addition, in this section, the true is numerically calculated using the modified profile.

3.1 The SST Experiment Description, Setup and Process

The purpose of the SST experiment is to test four different detection algorithms on a very dim, but known space object so that the relative performance of different detection algorithms can be compared in a controlled environment [29]. The four detection algorithms are the point detection and correlation detection, and MHT_6 and MHT_{10}. In this experiment, the MHT_6 and MHT_{10} are chosen because performance of the six versus ten hypotheses will illustrate the advantage or disadvantage of increasing number of hypotheses.

As described in [29], in order to perform this experiment the GEO communication satellite ANIK-F1 going in and out of eclipse during the 2012 vernal equinox is used. Although there are many cataloged dim astronomical objects, the eclipse scenario with a GEO satellite was

chosen for number of reasons. First, this particular scenario was picked because the unresolvable satellite body experiences continuous and gradual reduction of solar illumination, which provides a range of intensity values where different algorithms can be used to test for the performance. Second, since the presence and location of the satellite is known and easily established when it's fully illuminated, such that all detection algorithms can detect the object before going into eclipse. Third, with the telescope pointed directly at the satellite (pre and post eclipse), the presence of the satellite is known. Therefore the algorithm used to test the performance can be considered to be ascertained in a controlled environment. Fourth, with object being known or present during the eclipse, a firm conclusion can be established in actually detecting an object with a higher success rate versus false detection. Finally, because the object is located in GEO, it's relatively stationary in the sky therefore, no tracking motion from the telescope's motor is necessary [29].

Collections of the raw data were obtained over six different nights [29]. During each night of the experiment, images of the night sky with ANIK-F1 centered in the FOV were collected using 100ms exposures at a rate of one frame per second. Since the detection algorithms are to be tested on a single object, the window of 19 by 19 pixels around ANIK-F1 is used in the end.

Although ANIK-F1 is relatively stationary, there still is movement due to small orbital perturbations. This movement causes sub-pixel motion of the object on the CCD array as shown in Figure 19, which has a blurring effect when averaged over a multiple frames.

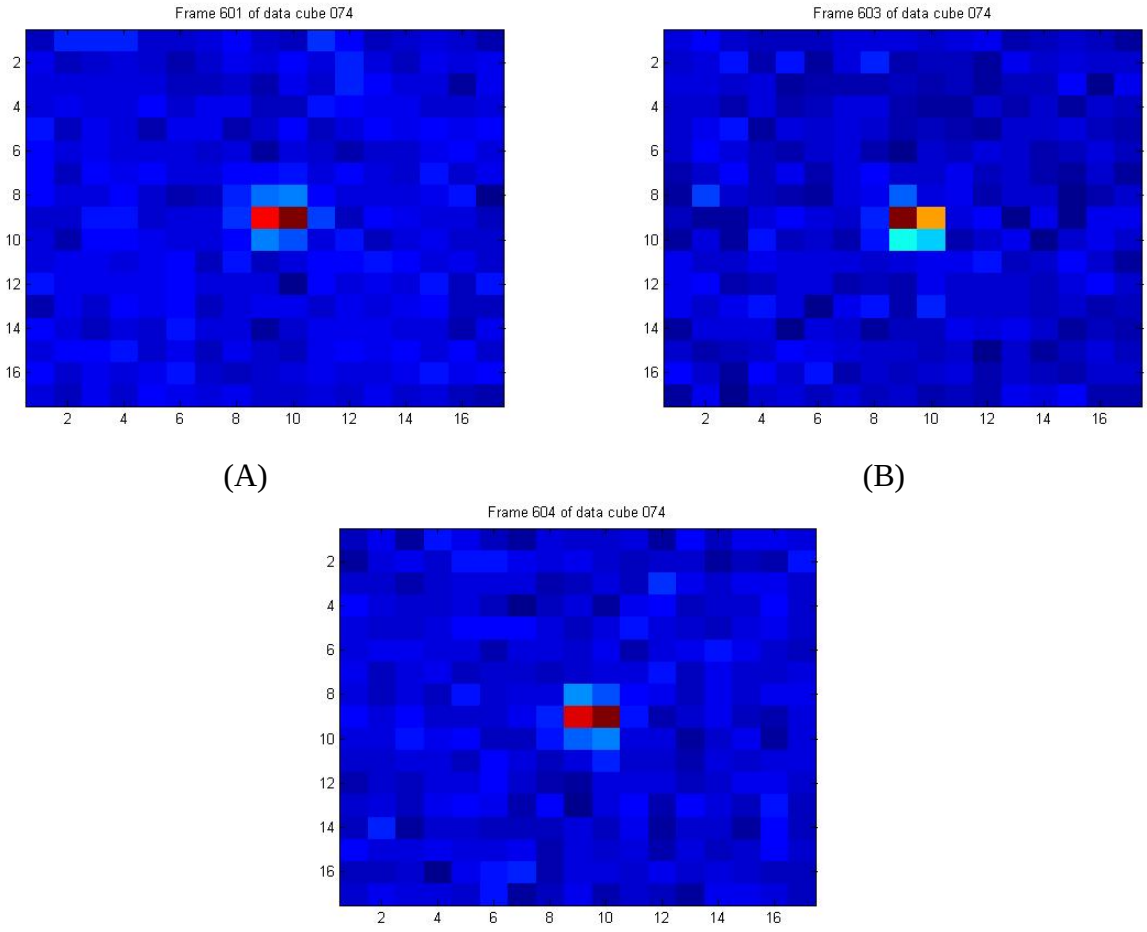

Figure 19. Sub-pixel motion due to orbital perturbations (14 Mar 2012 dataset). (A) Image of PSF w/ frame number 601 (B) Image of PSF w/ frame number 603 (C) Image of PSF w/ frame number 604.

The performance of all algorithms will suffer as a result because object is not located in center pixel, with the point detection algorithm being affected the most. To correct this problem, the two-dimensional match filter technique was utilized. The shift operations in the SST telescope model were then replaced with the match filter technique. To obtain more accurate results, a two-dimensional match filter tested surrounding pixels around the center pixel (total of 9 pixels) for the best fit model as shown in Figure 20.

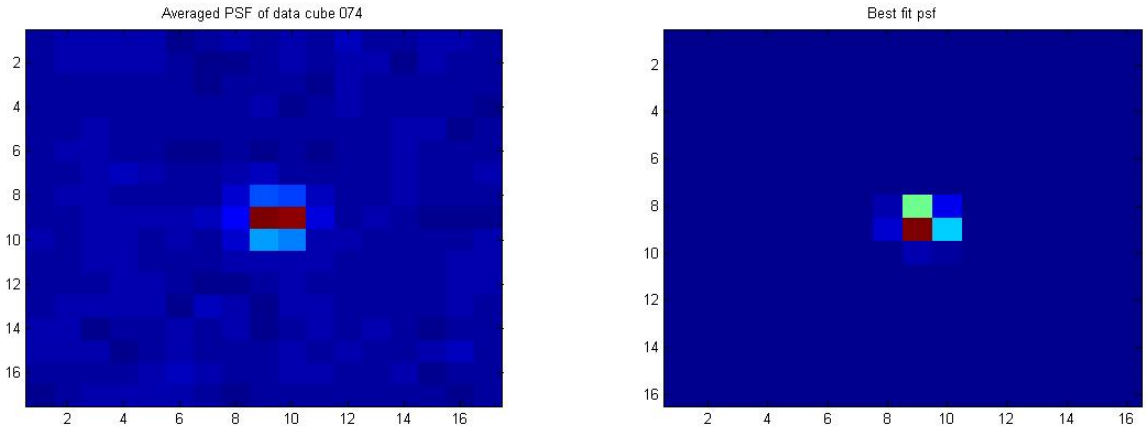

(A) (B)

Figure 20. (A) Image of PSF averaged out using 12 frames (B) Image of best fit PSF (both using 14 Mar 2012 dataset), showing the difference in PSFs.

In order to properly generate the PSF, the atmospheric seeing parameter must be determined first. This was accomplished by comparing the PSF of the observed data against the simulated PSF within range of atmospheric turbulence seeing values. However, a problem was encountered with this approach because although an object in the GEO is considered relatively stationary, there still is a small movement due to the orbital perturbation. This motion of the object must be considered when comparing PSFs. To account for the motion, nine different PSFs in nine different positions was simulated and compared against the observed data. Then the MSE calculation was performed to determine the best fit data.

With the seeing parameters determined, the next step is to extract the PSF from the images used to test the four different detection algorithms. First, the point detection or baseline detection currently used by the SST does not require a PSF because it only analyzes the data just within a single pixel to make detection decision. Second, the correlation or matched filter detection algorithm currently used by the Pan-STARRS program requires the use of a PSF [43]. The correlation detection algorithm does not consider undersampling or sub-pixel motion,

therefore a single empirically measured PSF can be used on this particular detector. Third and fourth, with the MHT_6 and MHT_{10} a properly sampled PSF must be generated. As discussed in Section 2.3, this is so that the PSF shape for the different hypotheses used in the test corresponding to the different sub-pixel locations can be generated [29].

The threshold value of the SST's point detection algorithm and the correlation detection algorithm are calculated to be , and the threshold value of the MHT_{10} is calculated to be .22 [29]. By using Eq. (22) derived from [29], the MHT_6 is calculated to be .11. For Eq. (22), two simplifying assumptions are made to find the upper bound of the for the 5-ary test. The first is considering for each alternative hypothesis of the 5-ary test to be mutually exclusive such that . The second assumption is that the result of each individual alternative in 5-ary test is statistically independent of each other. Under those two conditions the can be found [29].

(22)

In the MHT, the overall SNR increases due to the fact that additional hypotheses are tested. This causes the estimated for the M-ary test to change. To compensate, the SNR threshold must be raised in order match the BHT's using a SNR threshold of 6. In the 5-ary test, this can be accomplished by raising the detection threshold, .

To produce plots, running averages with a 40 frame window for the baseline detector SNR, , the correlation detector SNR, , 5 –ary test detector SNR, , and 9-ary test detector SNR, , were found in the threshold region all four detectors. The purpose of implementing running averages was used to reduce the effect of noise as illustrated in Figure 21.

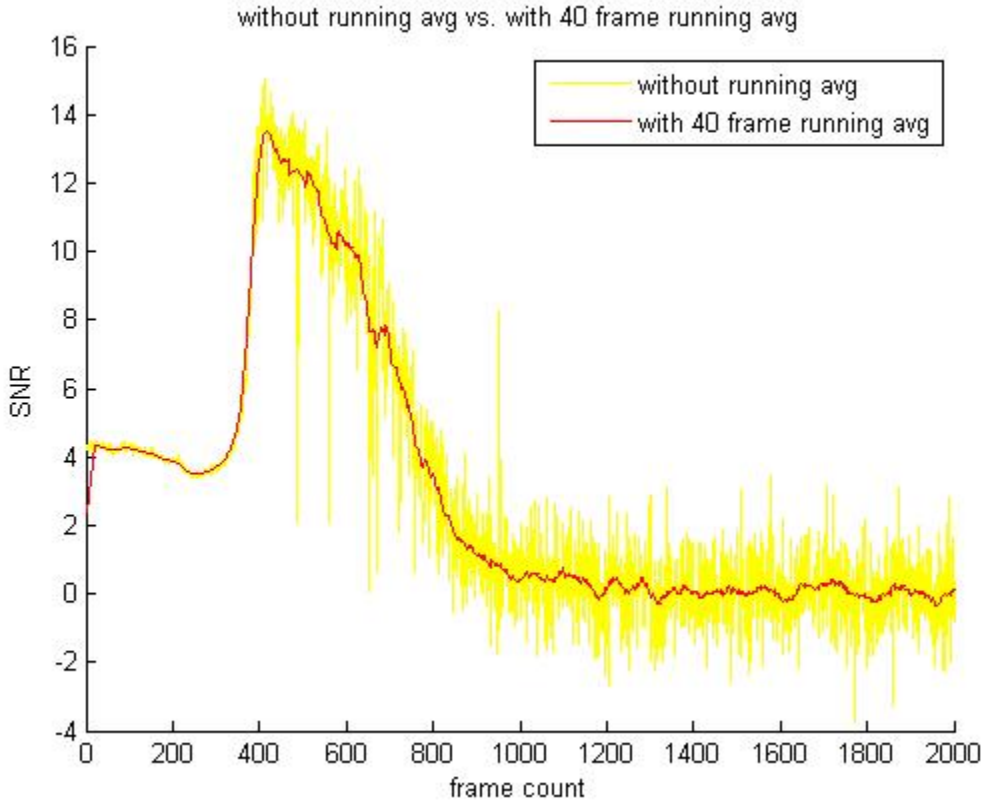

Figure 21. Baseline detector with 40 frame running average versus no running average.

The probability of detection for the baseline detector, , correlation detector , , 5-ary test detector, , and 9-ary test detector, , are found as a function of running average as show in Eqs. (23-26), which based on the Gaussian *Probability Density Function* (PDF) noise assumption [25].

(23)

(24)

(25)

(26)

When plotting the probability of detection versus frames, the initial point or starting frame is unknown. According to the survey of GEO satellite glint event proceeding conducted by the *United States Naval Observatory* (USNO), the satellite reaches peak illumination point just moments before it enters into ellipse followed by gradual reduction in solar illumination as shown in Figure 22 [44]. Hence, ideally the frame with the highest followed by gradual reduction is the initial point which can be used in plotting the graph.

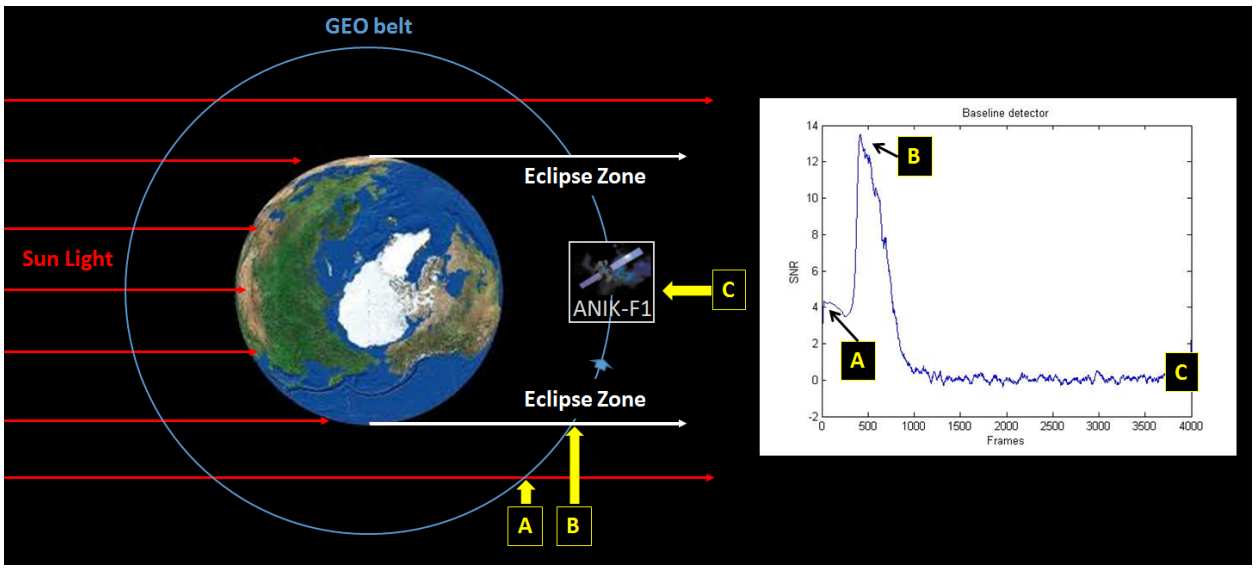

Figure 22. Eclipse experiment overview. Point (A) is prior to entering the eclipse. Point (B) is moment just before entering the eclipse. Point (C) is deep in the eclipse (plot generated using 14 Mar 2012 dataset). (Note: objects not to scale)

Using Eqs. (23-26) is valid method of creating the SNR curve, however its incorrect way of determining the initial point of an object before it enters the eclipse, also known as the terminator. The use of the SNR curve is found to be inaccurate because number of factors such as the noise spike, star crossing, PSF blur, weather, motion or rotation of satellite itself, and/or other anomalies can fluctuate the SNR. This fluctuation can cause the peak SNR to occur elsewhere, resulting in a false terminator. Selection of a false initial point will create an inaccurate result when testing the performance of the detection algorithms. Thus, actual initial point must be determined which can be found by plotting an averaged total PSF intensity within a set window size (11 by 11) instead of using the SNR curve as illustrated in Figure 23.

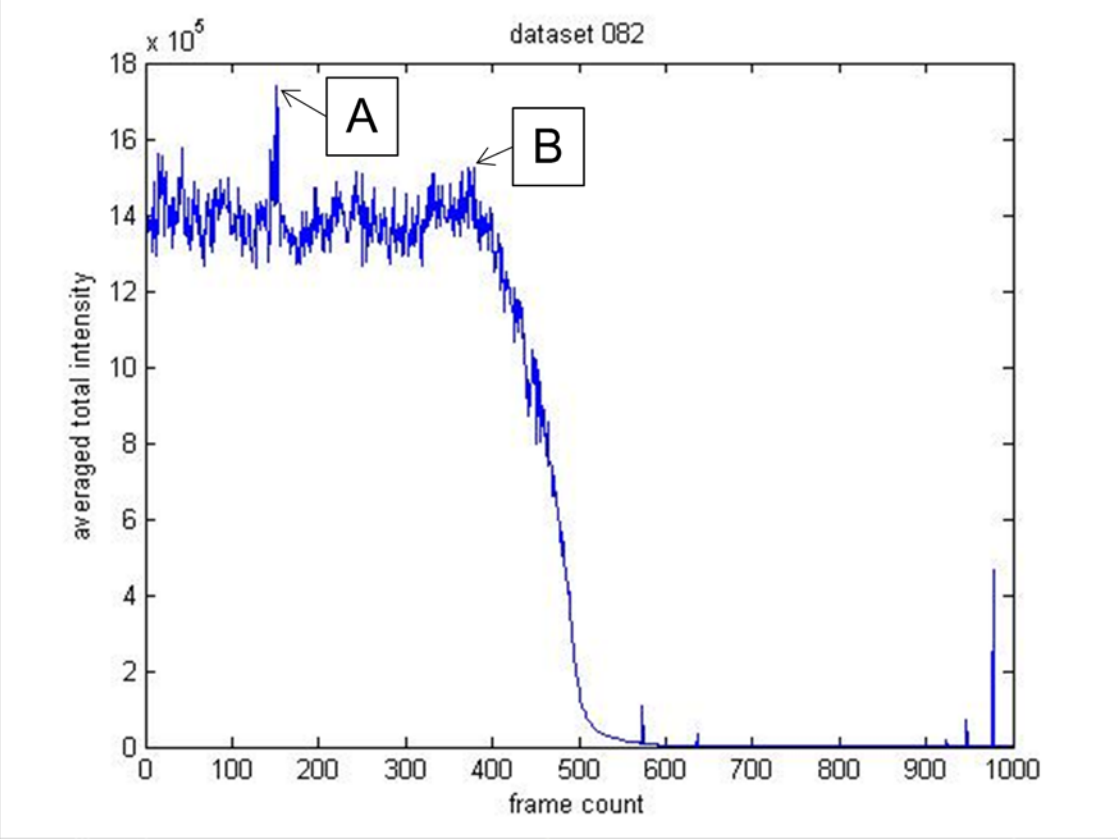

Figure 23. Averaged total intensity for dataset observed on 22 March 2022. Point A, represents false peak intensity. Point B, represents true peak intensity.

Examination of the averaged total PSF intensity of the dataset observed on 22 March 2012, shown in Figure 23, reveals that if the SNR curve was used to find the initial point, it would select the point A. However, the point A is a false initial point because the plot illustrates that after the point A, averaged intensity increases until the point B. If the point A is the actual initial point, averaged total intensity should have started to decline as it did after the point B. Thus, the point B is the true initial point, which coincides with the USNO's glint study. The analysis of the dataset suggests that the peak intensity at point B in is most likely caused by the noise spike within the CCD.

Hence, determining the peak intensity corresponding to the initial point is crucial in obtaining an accurate result for performance of the detection algorithms. Selecting a false initial point would result in an inaccurate result as shown in Figures 24A and Figure 24B. Figure 24A, illustrates using the peak SNR for each detection algorithm results in plots that are unsynchronized with no common initial point. Figure 24B, illustrates using a synchronized or common initial point for each detection algorithm.

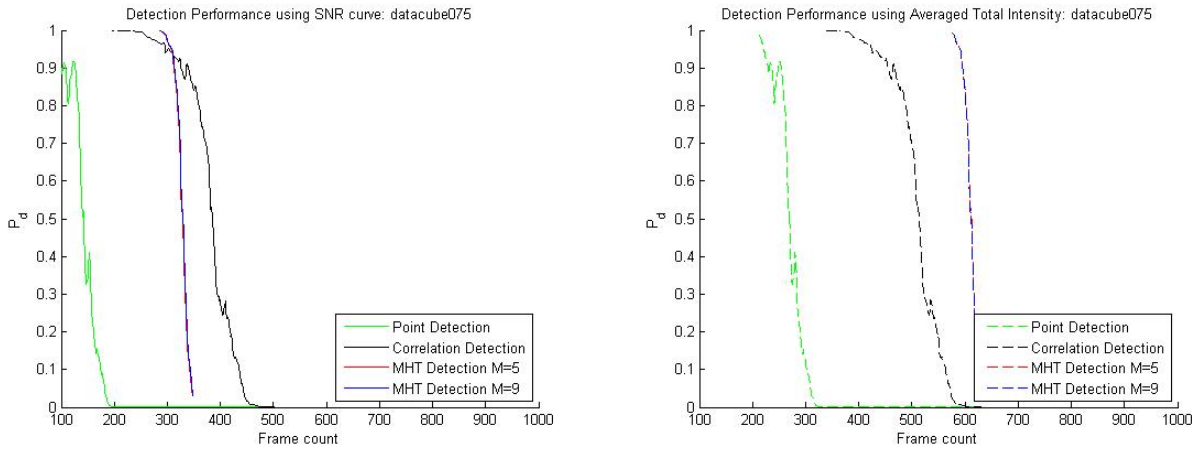

(A) (B)

Figure 24. Detection performance using dataset observed on 15 March 2012. (A) The performance result using peak SNR (shown as point A in Figure 23) for each detection algorithms, which illustrates unsynchronized plots (B) The performance result using true initial point (shown as point B in figure 23) for each detection algorithms, which illustrates synchronized plots.

Furthermore, determining the true initial point is an essential procedure when comparing results from two different datasets. In addition to the number of factors mentioned previously, because different datasets have different parameters for that particular day of observation (i.e., seeing value, weather, and etc...), the use of the SNR curve for determining the initial point for the comparison would be unreliable and an incorrect method.

Thus, using an averaged total intensity should be considered more accurate and reliable method of finding the initial point because it's not a function of either the PSF blur or standard deviation of noise; therefore it does not get influenced by factors that affect the SNR curve.

3.2 The AFIT Telescope Experiment Description, Setup and Process

Properly characterizing the atmospheric model is crucial in determining the performance of the GBO system because it is one of the limiting parameters as discussed in Section 2.2. To perform this experiment, a set of data of a space object was needed in order to proceed. Polaris, also known as the Northern Star, was chosen to be observed because it is very bright and easy to locate from the Northern Hemisphere. The AFIT back parking lot was chosen as the data collection site and data was collected on 14 August 2014. Images of the night sky with Polaris in the FOV were collected using the 1s exposure at a rate of 1 frames per second within raw 512 by 512 pixel image.

Although it looks stationary in the naked eye when observed for short period, just like any other stellar object, the motion of the Polaris is observed in CCD array due to Earth's rotation. As discussed in 3.1, this is an issue because it has blurring, in this case a streaking effect, when averaged over multiple frames as shown in Figure 25A. As implemented in the SST

system model, match filtering or a shift operation was used to correct this problem as shown in Figure 25B. However, the difference between the two is that the shifting operation was implemented at the very beginning because the MHT algorithm is not being tested for this experiment.

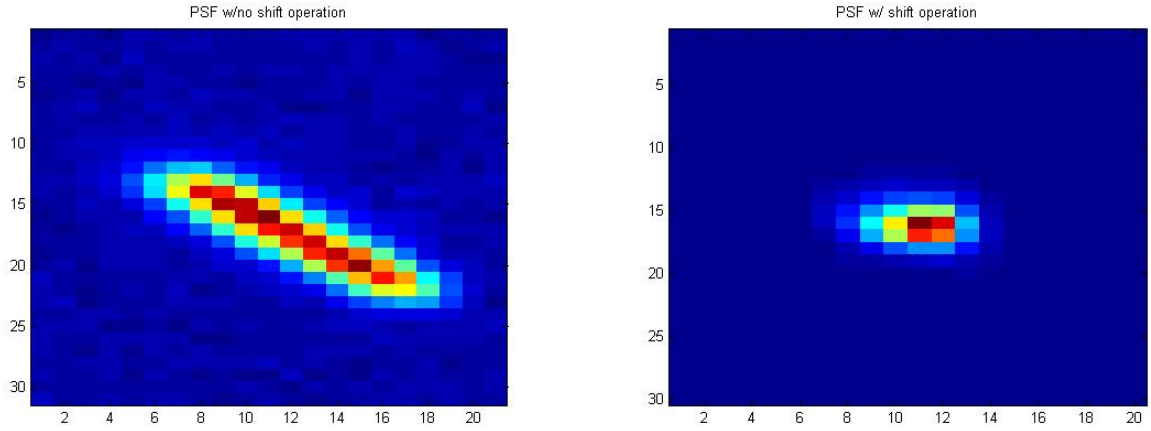

(A) (B)

Figure 25. (A) Image of PSF no shift operation (B) Image of PSF with shift operation.

With shift operation in place, the observed data can be processed and the PSF can be extracted by following the process described in Section 2.1.2. The PSF of the observed data then can be compared against the PSF over a range of simulated atmospheric turbulence and the best fit model can be determined via the MSE technique. An estimated can be obtained from using the MSE calculation. An estimated value obtained from the AFIT telescope experiment can then be converted to match the SST's via scaling factor which will be discussed in Section 4.2.1.

Lastly, using the estimated as the atmospheric seeing parameter, the performance of four detection algorithms can be tested using the AFIT telescope dataset. The dataset with the 25ms integration time was selected. Although the AFIT dataset with the 10ms integration time is available, it will not be used due to the excessive background noise. Results will be plotted

using the *Receiver Operating Characteristic* (ROC) curve in Section 4.2.2, because the AFIT telescope experiment did not observe an eclipsing event like the SST's experiment.

3.3 Seeing Parameter using Modified Hufnagal Valley

The purpose of this section is to numerically calculate the atmospheric seeing parameter, using the profile described in Section 2.2.5. To accomplish this, first the calculated value of using the profile is compared against the measured at Socorro, New Mexico and Exmouth, Australia. This was done to check the validity of the profile at that given location. Comparison revealed that for Exmouth, Australia, results were fairly accurate (5cm measured vs. 4.78cm calculated), therefore for this experiment, the profile are assumed to be valid at this location. However, for Socorro, New Mexico, results were significantly different (8cm measured vs. 6.8cm calculated), which suggests that profile is invalid for this location. Therefore a modified profile must be obtained to calculate for . In order to obtain a modified profile, for the — coefficient term in the model versus at Soccorro, New Mexico, was plotted to determine the correct coefficient values as shown in Figure 26.

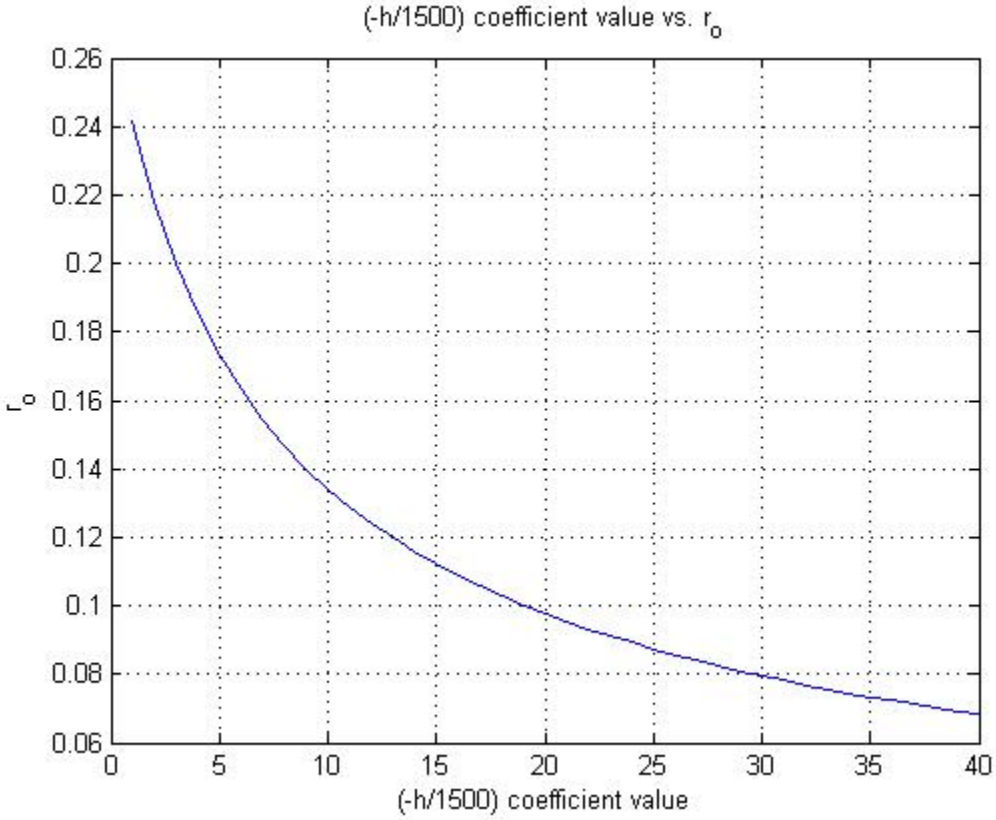

Figure 26. Coefficient for —— vs. at Socorro, NM.

The plot reveals for , the matching coefficient for the —— term is . Modified profile, Eq. (27), was created using newly obtained coefficient value.

— —— —— — (27)

where is the elevation of viewing site described in Eq. (18).

The difference between the profile, Eq. (18) and the modified profile, Eq. (27), is that only the mid profile was changed. This is because since Socorro, New Mexico, is located in elevation of 1,396m, the value of the profile at low altitude, which has

most atmosphere with greatest effect becomes negligible. And the value of the profile at high altitude, which has least atmosphere, is so small that it does not dramatically affect the result. With the modified profile, can be calculated using Eqs. (19-20).

3.4 Conclusion

This section described the experiment description, setup and processing for the SST and AFIT telescope experiments. For the SST experiment, the reasoning behind observing ANIK-F1, the blurring effect caused by the motion, a method of correcting the error via match filter technique, purpose of implementing the running average, calculating the SNR threshold, and the glint effect was described. For the AFIT telescope experiment, implementation of the shift operation to extract the PSF was discussed. Additionally, a method of obtaining and calculating the seeing parameter numerically using modified profile was discussed in this chapter

In next chapter, for the SST model, four different detection algorithms will be tested to determine the best performing algorithm in detecting a dim object in space. Graphs will be plotted using the probability of detection for all detection algorithm based on the Gaussian noise assumption. For the AFIT telescope experiment, the estimated will be converted using the scaling factor and performance of the detection algorithms will be tested using the AFIT telescope dataset. Additionally, the seeing parameter calculated numerically using the profile and modified profile will be compared against analytical results obtained from the SST datasets.

IV. Results and Analysis

This section presents the results of applying the algorithms developed in *Chapter II and III* to both the simulated and measured data sets for the SST and AFIT telescope experiment. For the SST experiment, performance of four detection algorithms will be compared. For the AFIT telescope experiment, the value obtained from the measured data will be scaled to match the SST system. Using the estimated as the atmospheric seeing parameter, performance of the detection algorithms will be tested using the AFIT telescope dataset.

Also, results for the atmospheric seeing parameter, value for Socorro, New Mexico and Exmouth, Australia that was numerically calculated using modified profile. Additionally, the SST datasets with the value closest to the numerically calculated value will be selected and compared. This simulates the SST's performance for both locations and differences can be compared.

4.1 Performance of Detection Algorithms for the Space Surveillance Telescope

In the SST experiment, the atmospheric seeing parameter, , value for each dataset were first obtained using the technique discussed in Section 3.1. Using analyzed values (listed on Table 5), the performance of the point detection, correlation detection, MHT_6 and MHT_{10} were tested. In this experiment, the detection algorithms did not utilize the outlier technique discussed in Section 1.4.

Table 5. values of datasets.

Dataset	value
13 Mar 2012	5.9cm
14 Mar 2012	6.1cm
15 Mar 2012	5.6cm
21 Mar 2012	3.5cm
22 Mar 2012	4.8cm
23 Mar 2012	6.4cm

4.1.1 Dataset observed on 13 March 2012

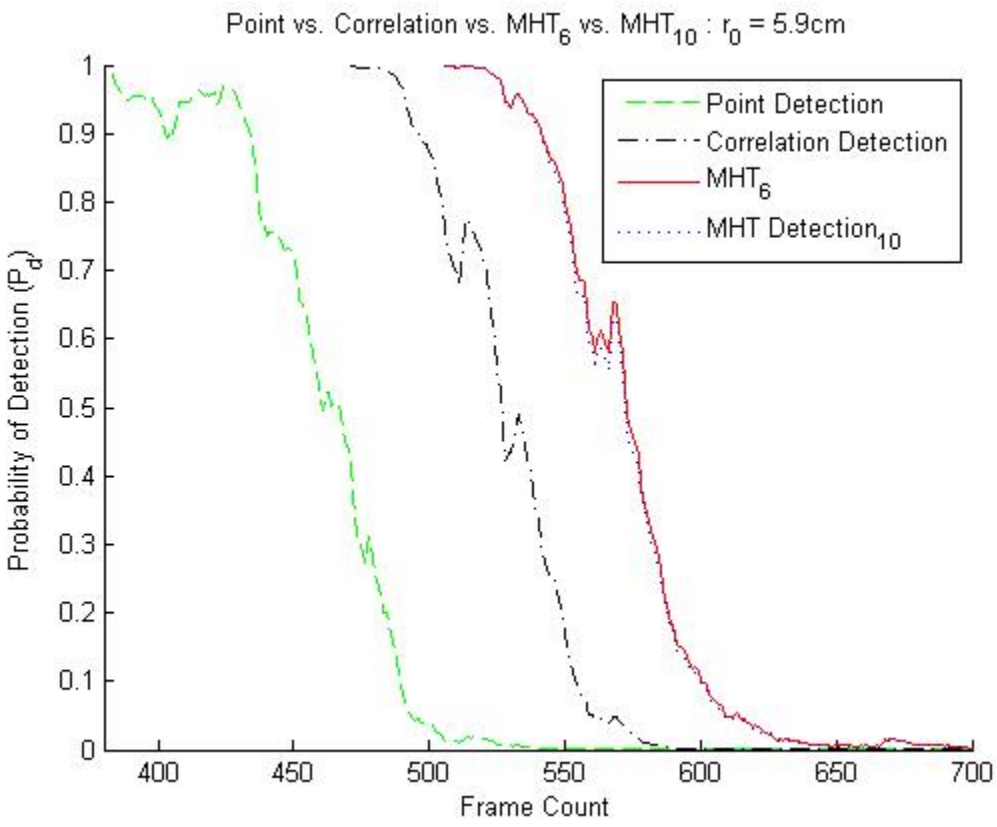

Figure 27. Performance of detection algorithms for 13 March 2012 dataset.

The performance of four detection algorithms for the SST dataset observed on 13 March 2012 is shown in Figure 27. The result illustrates that MHTs clearly outperform BHTs, and the MHT_6 very slightly outperformed the MHT_{10}. This result for MHTs coincides with MHT detection theory as discussed in Section 2.3.

Detailed analysis and comparison of algorithm performances revealed that when the baseline algorithm has , meaning that half of the time it detects an object, and half of the time it doesn't, other three detection algorithms has , meaning that it always detects. When the baseline algorithm has , meaning that if is 4% chance it detects an object,

correlation algorithm has , and MHT algorithms has . Detailed analysis and comparison of algorithm performances are listed in Table 6.

Table 6. Comparison chart for detection algorithm performance using dataset observed on 13 March 2012

Point Detection (Baseline)	Correlation Detection	MHT_6	MHT_{10}

Intensity distribution of the dataset observed on 13 March 2012 is shown in Figure 28.

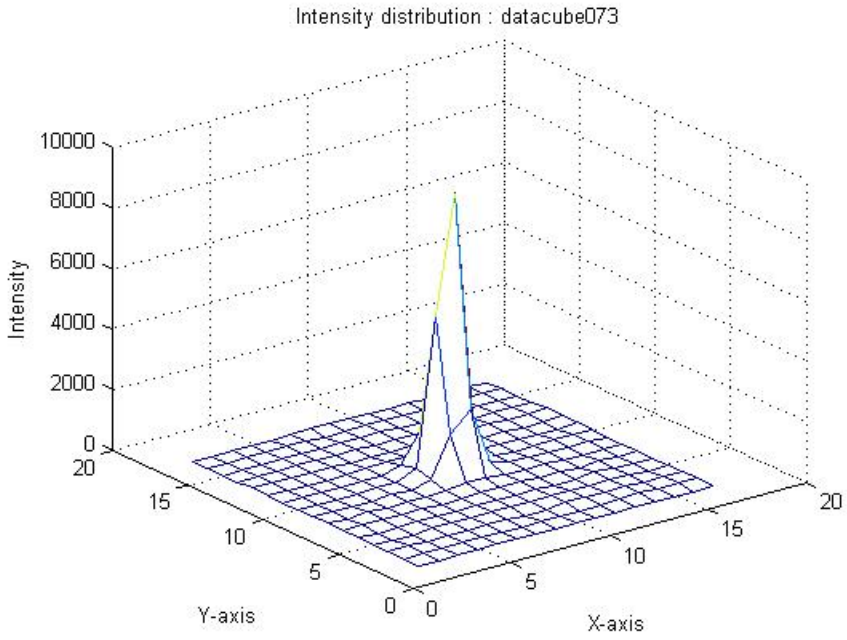

Figure 28. Intensity distribution of the dataset observed on 13 March 2012.

4.1.2 Dataset observed on 14 March 2012

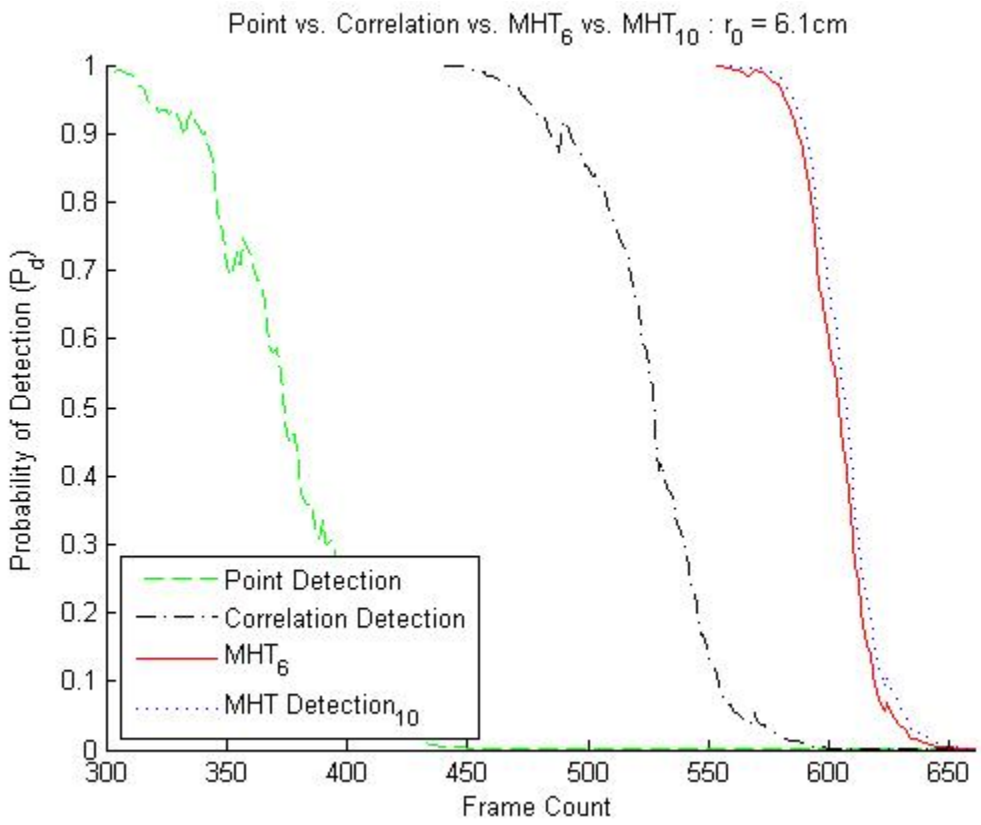

Figure 29. Performance of detection algorithms for 14 March 2012 dataset.

The performance of four detection algorithms for the SST dataset observed on 14 March 2012 is shown in Figure 29. The result illustrates that MHTs clearly outperforms BHTs, and the MHT_{10} slightly outperformed the MHT_6. Detailed analysis and comparison of algorithm performances are listed in Table 7.

Table 7. Comparison chart for detection algorithm using dataset observed on 14 March 2012

Point Detection (Baseline)	Correlation Detection	MHT_6	MHT_{10}

Detailed analysis of the plots reveals that the baseline algorithm for this dataset is considerably poor compared to other detection algorithms. In fact, the baseline detection algorithm for this dataset with , performs more poorly than the baseline algorithm from other datasets with a lesser value. This can be attributed to the position of the viewing object on the CCD. In this dataset, instead of being positioned in the center pixel, the object falls in-between sub-pixels. Additionally, the position of the object is constantly being shifted throughout the SNR threshold region. . This resulted in a wider intensity distribution over the adjacent pixel as shown in Figure 30. As a result of intensity distribution, the performance of the baseline drops significantly because the position of the object has the biggest effect on the performance of the point detection algorithm.

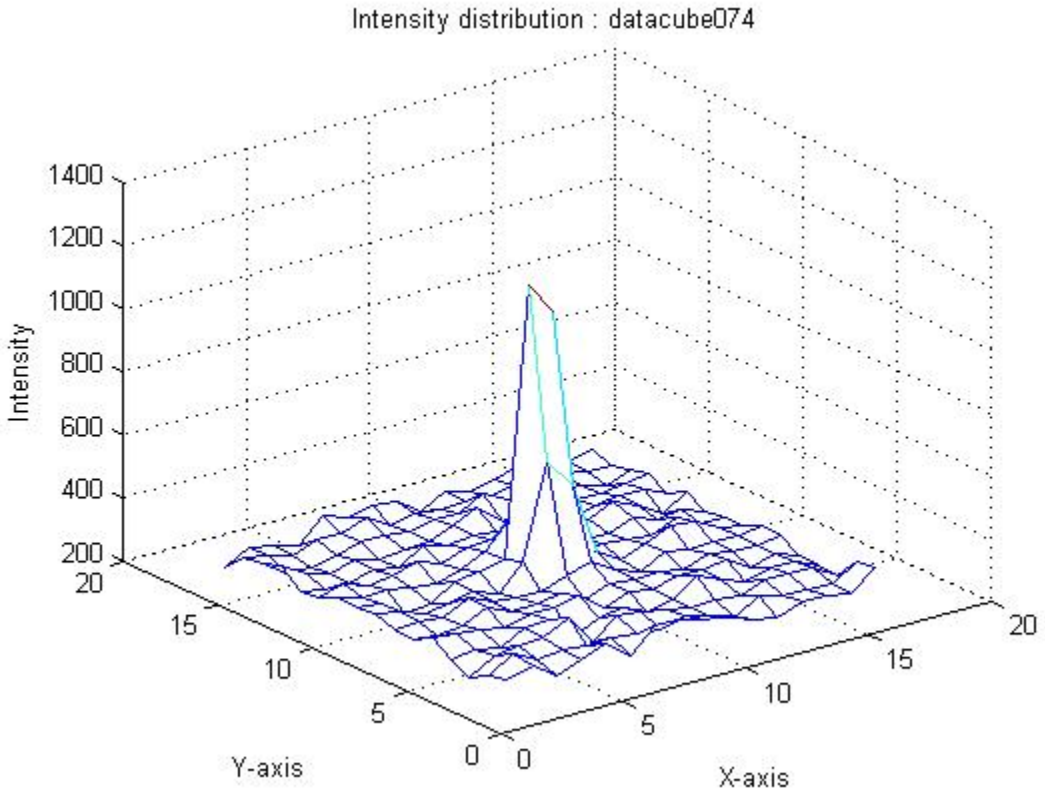

Figure 30. Mesh plot for intensity distribution of dataset observed on 14 March 2012.

4.1.3 Dataset observed on 15 March 2012

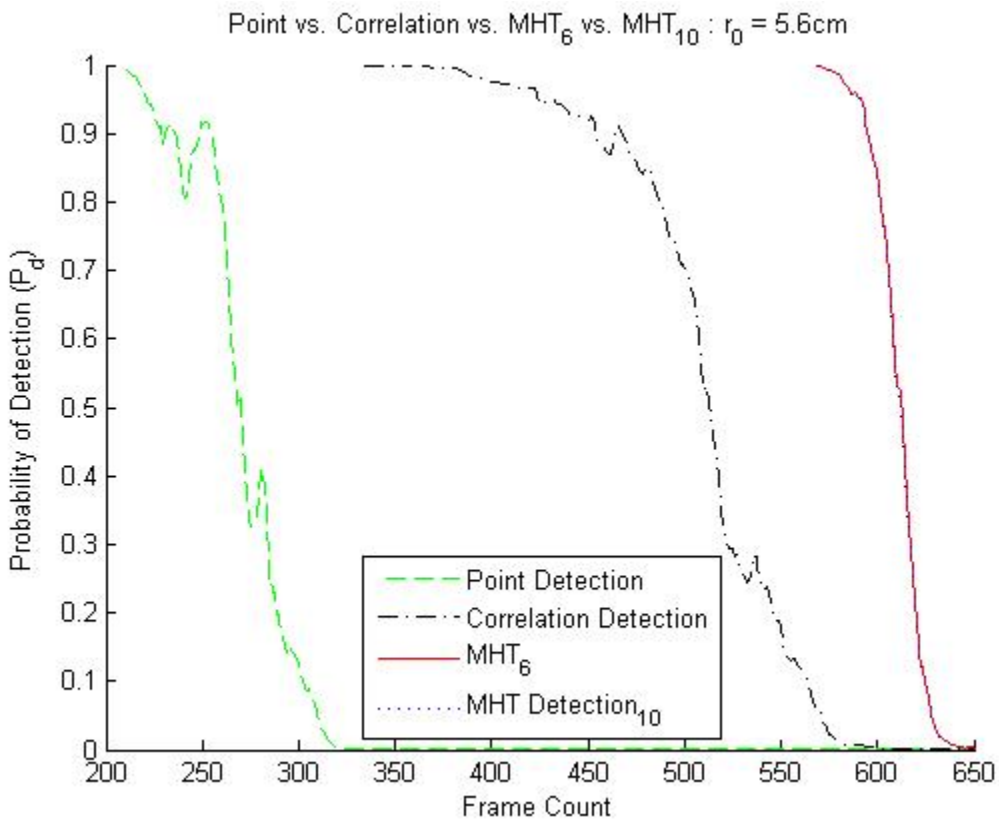

Figure 31. Performance of detection algorithms for 15 March 2012 dataset.

The performance of four detection algorithms for the SST dataset observed on 15 March 2012 is shown in Figure 31. The result illustrates that MHTs clearly outperforms BHTs, and the performance of MHT_6 and MHT_{10} were nearly identical, with the MHT_6 being slightly better. Detailed analysis and comparison of algorithm performances are listed in Table 8.

Table 8. Comparison chart for detection algorithm performance using dataset observed on 15 March 2012

Point Detection (Baseline)	Correlation Detection	MHT_6	MHT_{10}

Detailed analysis of the plots reveals that, just like in Section 4.1.2, the baseline detection algorithm for this dataset is considerably poor compared to other detection algorithms. In fact, the baseline algorithm for this dataset with , performs poorest amongst all other datasets. As discussed in Section 4.1.2, this can be attributed to the position of the viewing object on the CCD. In this dataset, instead of being positioned in the center pixel, the object falls in-between sub-pixels. Additionally, the position of the object is being constantly shifted throughout the SNR threshold region. This results in a wider intensity distribution over the adjacent pixel as shown in Figure 32. As a result, the performance of the baseline is very poor, as illustrated in Figure 31.

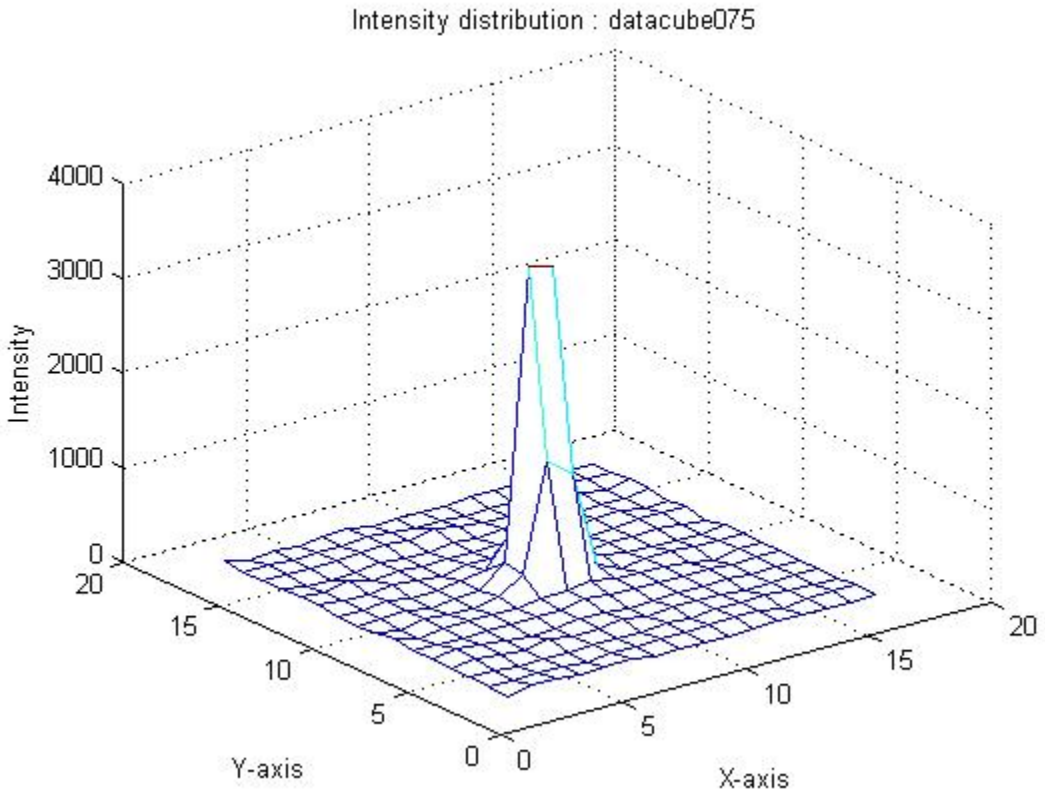

Figure 32. Mesh plot for intensity distribution of dataset observed on 15 March 2012.

4.1.4 Dataset observed on 21 March 2012

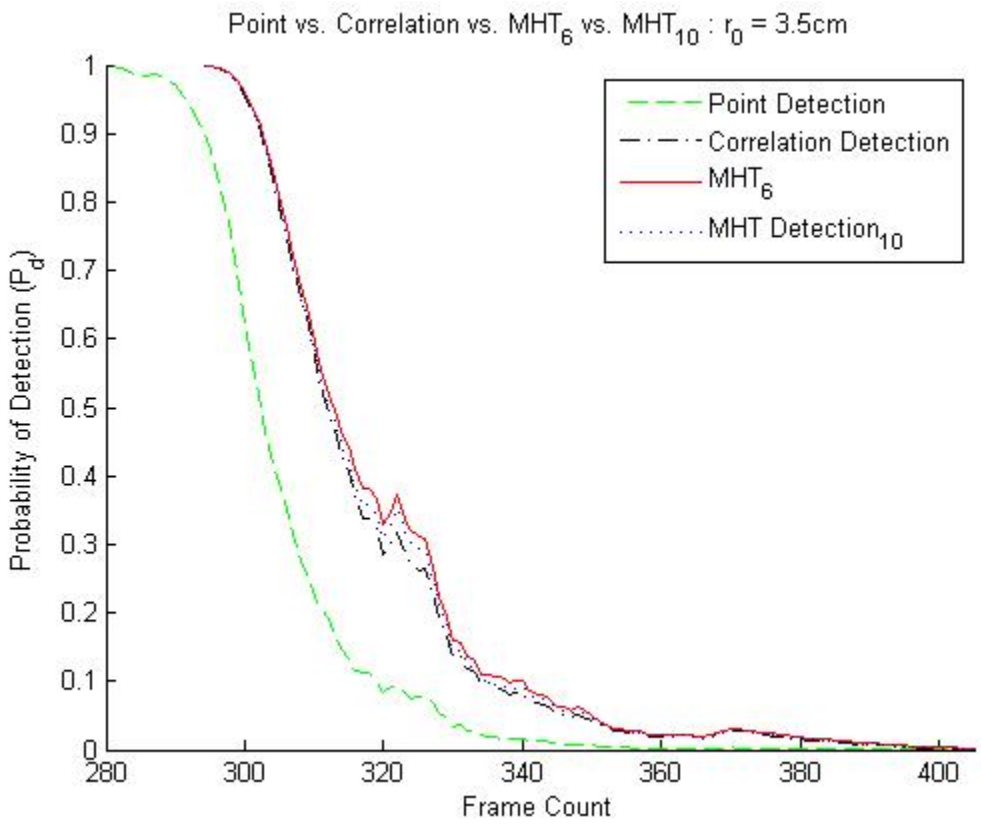

Figure 33. Performance of detection algorithms for 21 March 2012 dataset.

The performance of four detection algorithms for the SST dataset observed on 21 March 2012 is shown in Figure 33. The result illustrates performance of all four detection algorithms are much smaller than other datasets. Closer examination revealed that the MHT_6 performed the best, followed by the MHT_{10}, correlation detection, and point detection. This result for MHTs coincides with MHT detection theory as discussed in Section 2.3. Detailed analysis and comparison of algorithm performances are listed in Table 9.

Table 9. Comparison chart for detection algorithm performance using dataset observed on 21 March 2012

Point Detection (Baseline)	Correlation Detection	MHT6	MHT10

Plots illustrates that the performance difference for all algorithms are much smaller in this dataset. This can be attributed to both the position location of the object. In this dataset, the object was positioned in the center pixel and rarely moved throughout the entire dataset. This resulted in a concentrated intensity at the center pixel, as shown in Figure 34. It is theorized that the point detection, correlation detection, and MHT would perform equally when the position of the viewing object on the CCD is all centered, thus performance differences are much smaller in this dataset.

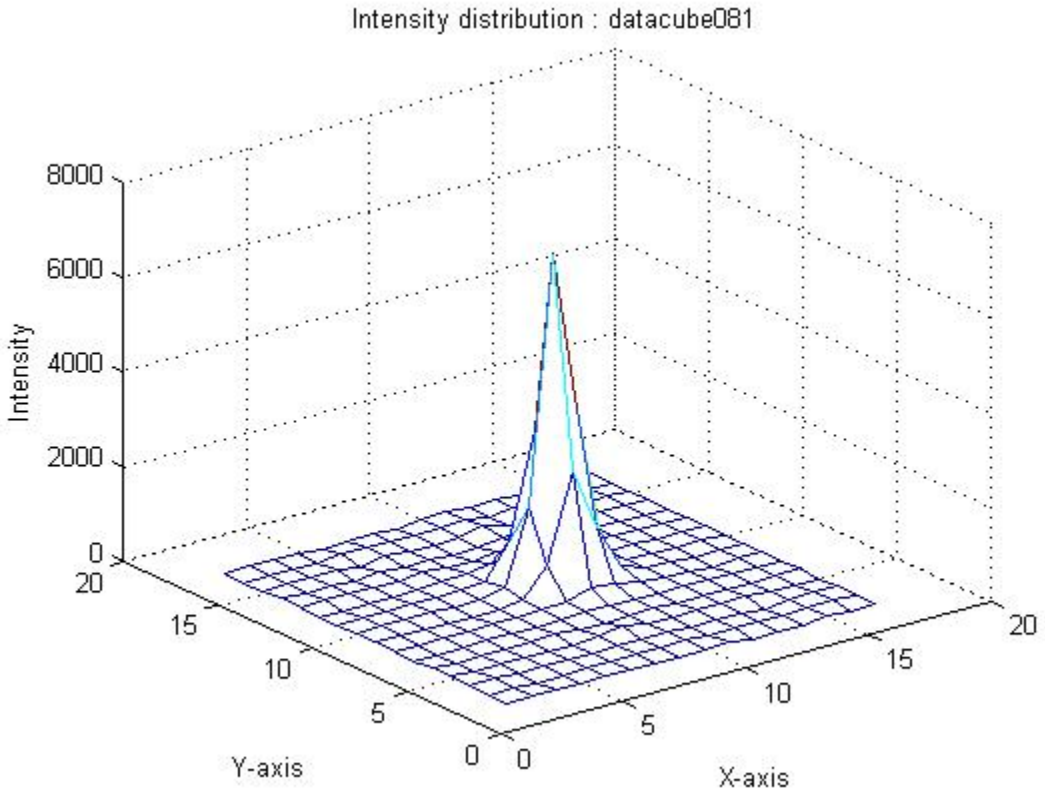

Figure 34. Mesh plot for intensity distribution of dataset observed on 15 March 2012.

4.1.5 Dataset observed on 22 March 2012

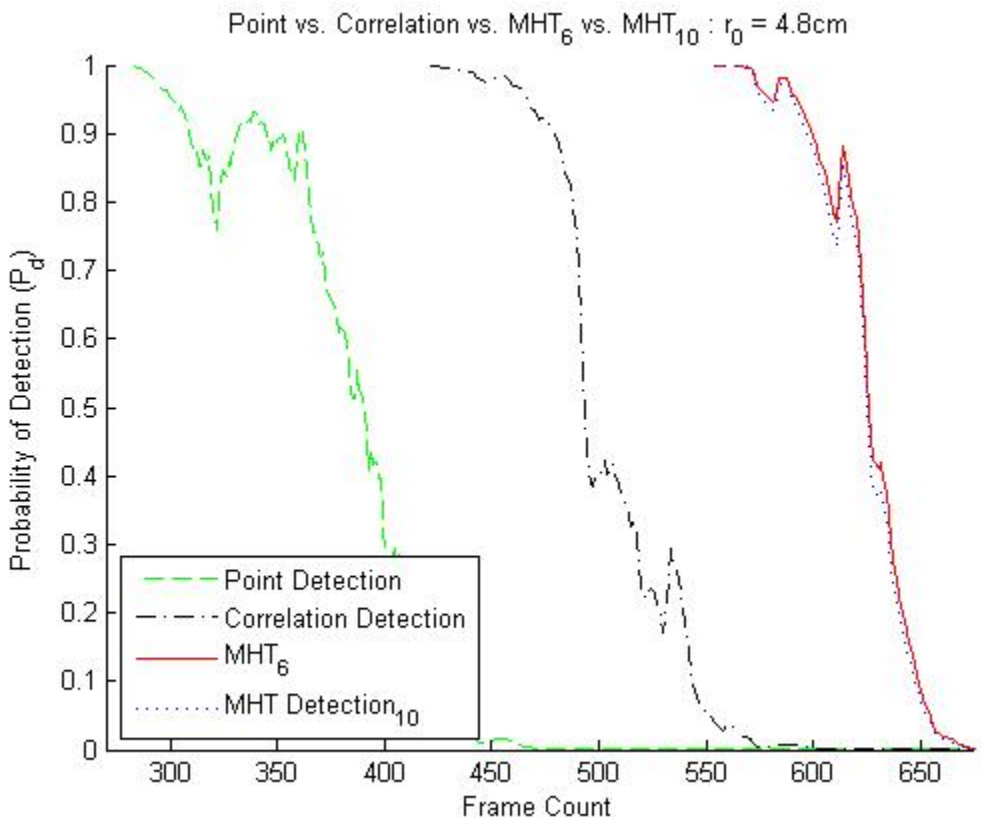

Figure 35. Performance of detection algorithms for 22 March 2012 dataset.

The performance of four detection algorithms for the SST dataset observed on 22 March 2012 is shown in Figure 35. The result illustrates that MHTs clearly outperform BHTs, and the MHT_6 very slightly outperformed the MHT_{10}. This result for MHTs coincides with MHT detection theory as discussed in Section 2.3.

Plot illustrates that the performance of the MHTs are exceptionally good for this dataset considering . In fact, MHTs from this dataset outperforms MHTs from other datasets with higher value. This can be attributed to position of the viewing object on the CCD. In this dataset, it's most likely that the object was positioned right on top of one of the hypotheses. This would result in MHTs outperforming other algorithms, because as discussed in Section 2.3,

position location determines the performance of the MHT. Detailed analysis and comparison of algorithms performances are listed in Table 10.

Table 10. Comparison chart for detection algorithm performance using dataset observed on 22 March 2012

Point Detection (Baseline)	Correlation Detection	MHT_6	MHT_{10}

Intensity distribution of the dataset observed on 22 March 2012 is shown in Figure 36.

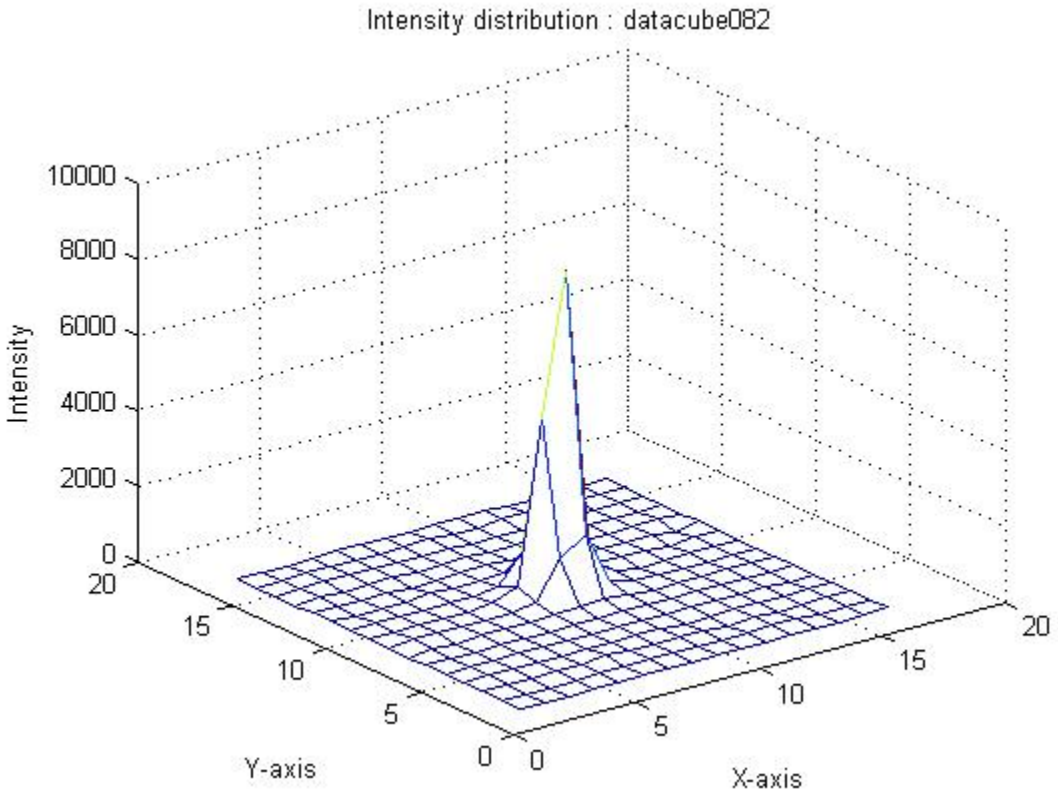

Figure 36. Mesh plot for intensity distribution of dataset observed on 15 March 2012.

4.1.6 Dataset observed on 23 March 2012

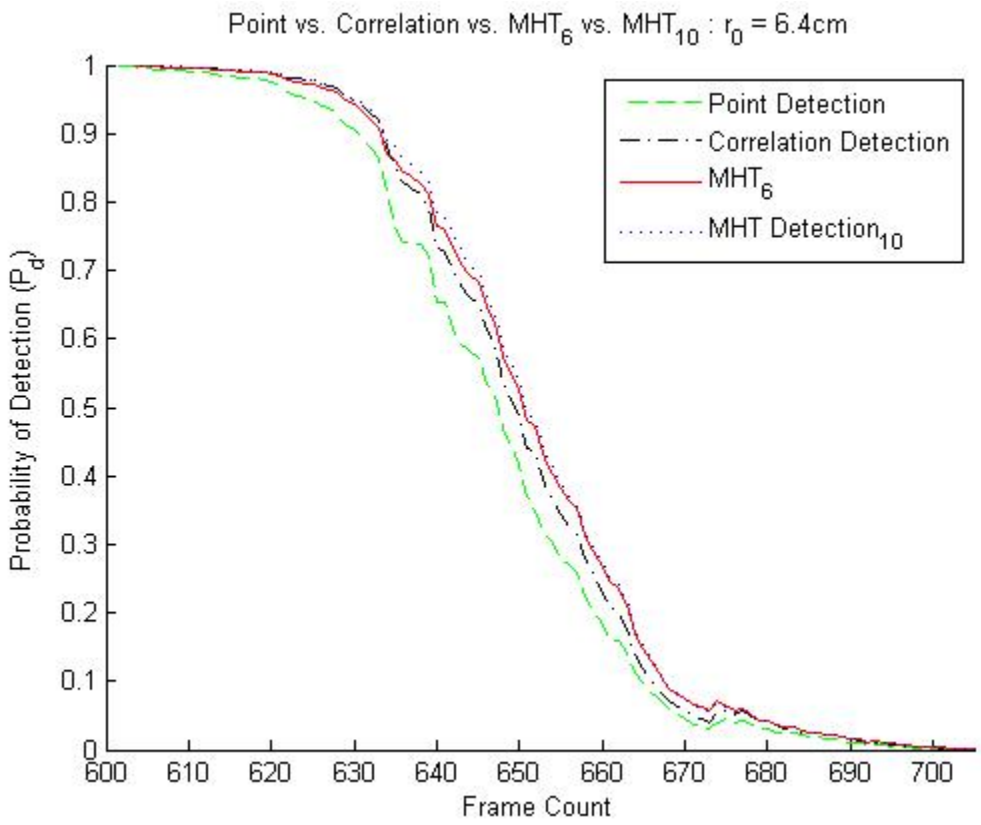

Figure 37. Performance of detection algorithms for 23 March 2012 dataset.

The performance of four detection algorithms for the SST dataset observed on 23 March 2012 is shown in Figure 37. The result illustrates performance of all four detection algorithms are very small. Closer examination revealed that the MHT_{10} performed the best, followed by the MHT_6, correlation detection, and point detection. Detailed analysis and comparison of algorithm performances are listed in Table 11.

Table 11. Comparison chart for detection algorithm performance using dataset observed on 22 March 2012

Point Detection (Baseline)	Correlation Detection	MHT_6	MHT_{10}

Plots illustrates that the performance difference for all algorithms were least in this dataset. This can be attributed to both the position location of the object and good seeing condition. In this dataset, the object was positioned in the center pixel and rarely moved throughout the entire dataset. This resulted in a concentrated intensity at the center pixel, as shown in Figure 38. It is theorized that the point detection, correlation detection, and MHT would perform equally when the position of the viewing object on the CCD is all centered, thus performance differences are the least in this dataset.

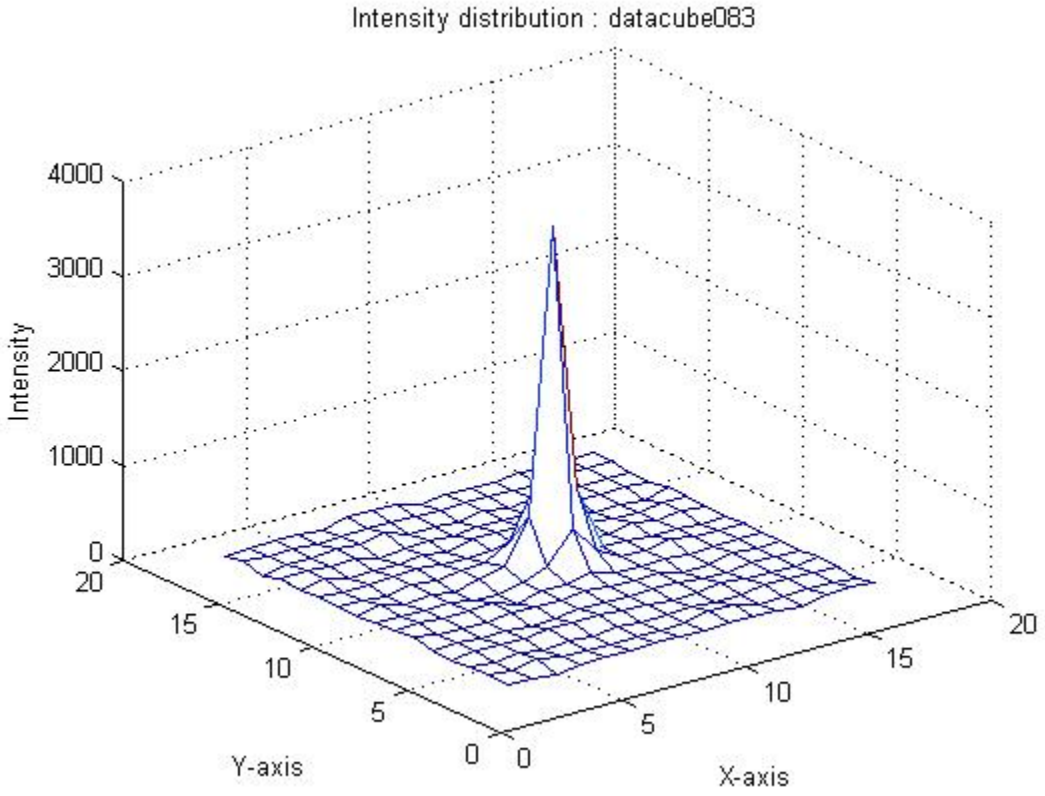

Figure 38. Mesh plot for intensity distribution of dataset observed on 23 March 2012

4.2 AFIT Telescope

4.2.1 Estimated and Scaled

As discussed in Section 2.1.2, the best fit PSF model was created from comparing the PSF of the observed data against the PSF for a range of simulated data. The averaged PSF was compared against the best fit PSF model as shown in Figure 39A-B. The MSE technique was used in the comparison to obtain the estimated value the , as shown in Figure 40.

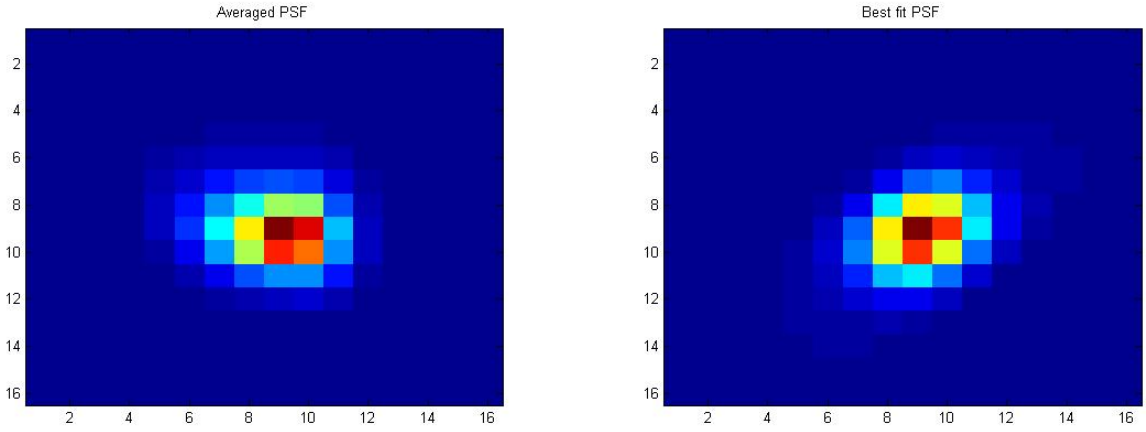

(A) (B)

Figure 39. PSF for AFIT telescope (A) Image of averaged PSF (B) Image of best fit PSF.

When looking at the image of the PSF in Figure 39A, the there is a higher concentration of intensity on the right bottom corner than other corners. This can be attributed to the star's movement towards bottom left corner, which caused the streaking effect as illustrated in Figure 25A. When the shift operation was conducted to obtain the averaged PSF, that movement caused higher intensity to be formed on the bottom left corner.

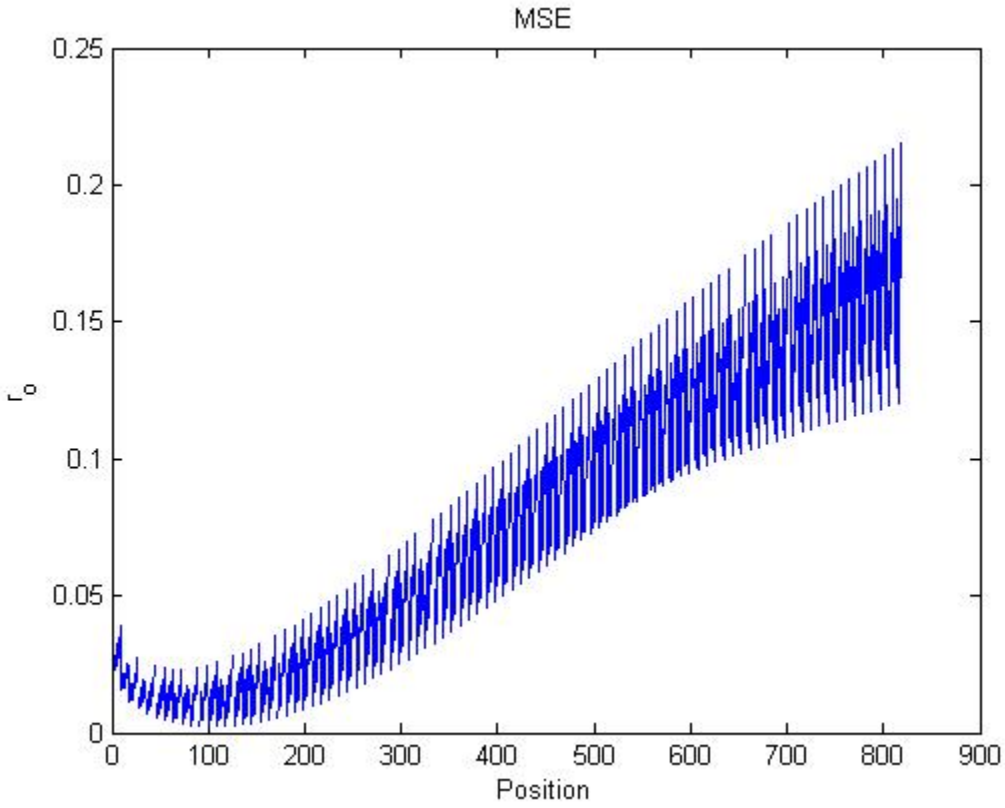

Figure 40. Obtaining value for AFIT telescope experiment via MSE technique.

An estimated , obtained from the AFIT telescope dataset, can now be scaled to match SST's. This scaled conversion was accomplished by scaling the AFIT telescope and SST's Nyquist sampling and undersampled factor as described in Eq. (9). By using the AFIT telescope and SST parameters listed in Table 2, a conversion formula, Eq. (28) was derived.

(28)

where is the SST's Nyquist sampling, is the AFIT telescope's Nyquist sampling, is SST's centered wavelength, is AFIT telescope's centered wavelength, is the SST's undersampled factor, is the AFIT telescope's undersampled factor, is the SST's CCD pixel size, is the AFIT telescope's CCD pixel size, is the SST's atmospheric seeing value, and is the AFIT telescope's atmospheric seeing value. By setting the undersampled factors, and equal, the can be calculated via scaled conversion. The scaled conversion yields . This is the seeing value that SST would have to be view through in order to obtain the performance similar to that of the results gained from the AFIT telescope experiment on this night particular night.

4.2.2 ROC Curve

Using the estimated obtained from the AFIT telescope experiment as the atmospheric seeing parameter, performance of four detection algorithms are tested using the AFIT telescope data. Unlike the SST experiment, the AFIT telescope experiment did not observe an eclipsing event. For that reason, the ROC curve was selected to represent the performance of detection algorithms. The ROC curve compares the probability of detection against the logarithm (base 10) of probability of false alarm, which is based on SNR, ranging from 0.005 to 10.

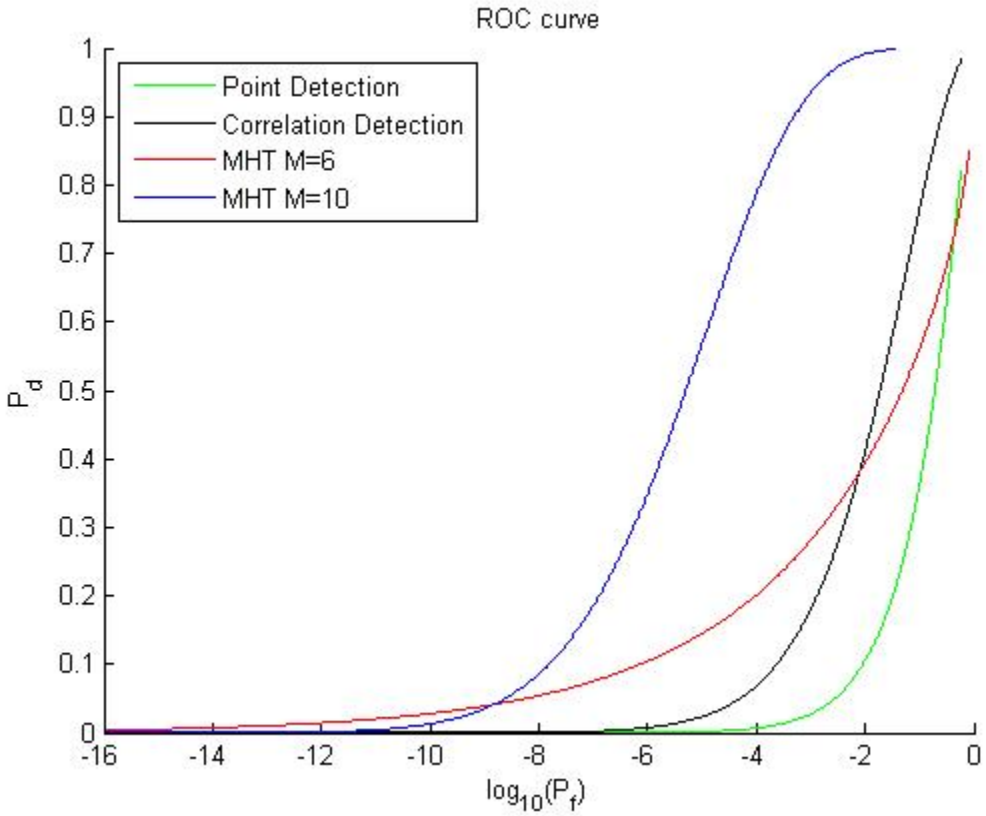

Figure 41. ROC curve for AFIT telescope dataset.

The performance of four detection algorithms for the AFIT telescope dataset using the ROC curve is shown in Figure 41. The plots illustrate that the MHT_6 and MHT_{10} crosses at the . This is point where the MHT_6 and MHT_{10} perform equally at the SST's chosen probability false alarm rate, which also validates results of MHTs obtained from the SST eclipse experiment in Section 4.1. The point where the MHT_6 and MHT_{10} crosses, , is approximately , which is the same value used to derived values of the SNR thresholds for and , calculated in Section 3.1 The plot illustrates that if the SNR threshold is raised, then the MHT_6 would perform better than the MHT_{10}.

On top of strengthening the fidelity of the analytical model for calculating the , the AFIT telescope experiment presents an additional set of tool, which can be used to test and validate the performance of SST's detection algorithms under very poor seeing conditions.

4.3 Seeing Parameter using Modified Hufnagal Valley Profile

In this Section, the averaged obtained analytically, MIT/LL's estimated , and results of the numerically calculated using both the and modified are listed in Table 12. Results indicate that for Exmouth, Australia, there is approximately difference between the numerically calculated value and MIT/LL's value. However, for Socorro, New Mexico, there is approximately difference between numerically calculated value and MIT/LL's value. As predicted, the difference between two results is far greater for Socorro, New Mexico because it's located further away from the equator, which coincides with the premise discussed in Section 2.2.4.

Table 12. Calculated vs. MIT/LL's vs. Analytical avg .

Location	Calculated	MIT/LL	Analytical avg
Socorro, New Mexico	6.8cm	8cm	5.4cm
Exmouth, Australia	4.78cm	5cm	N/A

4.4. Comparison

The purpose of the dataset comparisons is to predict the performance of the SST in Exmouth, Australia against Socorro, New Mexico by comparing the analytical against the numerical result. This can be accomplished first by setting the numerically calculated as the baseline . Averaging values obtained from the SST datasets yields , which indicates that analytical result is in more par with numerically calculated than the MIT/LL's estimation. Then values obtained from the SST dataset, listed in Table 5, were compared against the baseline . The comparison revealed that the dataset observed on 23 March 2012 (observed vs. calculated), best matched Socorro, New Mexico's seeing condition. And the dataset observed on 22 March 2012 (observed vs. calculated), best matched Exmouth, Australia's seeing condition. However, instead the dataset observed on 13 March 2012 (observed vs. calculated) was selected to simulate Socorro, New Mexico' seeing condition and dataset observed on 22 March 2012 was selected to simulate Exmouth, Australia's seeing condition. The selection of the datasets for the comparison was primarily based on the closest to the numerically calculated and the position location of the object recorded in these datasets.

It's important to understand that, in order to accurately and correctly compare the datasets, certain parameters of those dataset's must be met. Parameters are the position location of the object on CCD and its resulting intensity distribution. Analysis of datasets in Section 4.1, revealed that the object center position varied from dataset to dataset. And this variation in the position caused its intensity to be distributed differently as shown in Figure 28, 30, 32, 34, 36, 38. But if the differences in center position and its resulting intensity distributions are too large,

correct comparison cannot be performed. Therefore, the position difference must be the same or very similar in order to accurately and correctly compare the datasets.

Analysis of the dataset observed on 23 March 2012, which best matched Socorro, New Mexico's seeing condition and the dataset observed on 22 March 2012, which best matched Exmouth, Australia's seeing condition, revealed that discrepancies between the two datasets are unsuitable for comparison because the object center positions and intensity distribution is much different as shown in Figure 42.

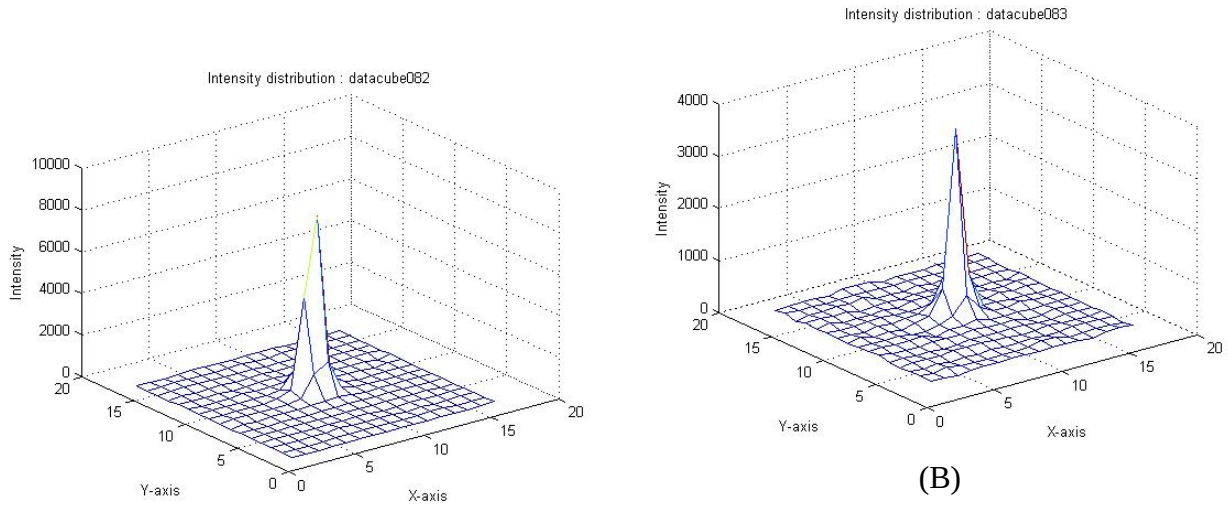

(A) (B)

Figure 42. Mesh plot comparison for intensity distribution (A) dataset observed on 22 March 2012 (B) dataset observed on 23 March 2012.

Analysis of dataset observed on 13 March 2012, selected to simulate Socorro, New Mexico's seeing condition and the dataset observed on 22 March 2012, selected to simulate Exmouth, Australia's seeing condition, revealed that two datasets were good candidates for a comparison because the object center positions and intensity distribution are nearly identical as shown in Figure 43.

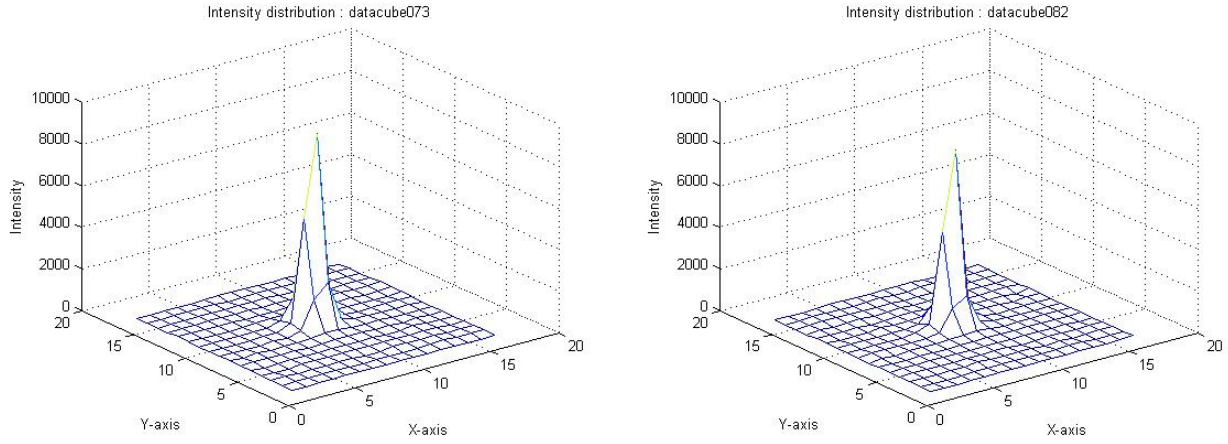

(A) **(B)**

Figure 43. Mesh plot comparison for intensity distribution (A) dataset observed on 13 March 2012 (B) dataset observed on 23 March 2012.

Due to the incompatibility of the dataset observed on 23 March 2012 for a comparison, the next best dataset available, the dataset observed on 13 March 2012 were used. The difference between values for the dataset observed on 23 March 2012 and new dataset observed on 13 March 2012 is approximately 6.2%, which fairly small and is within the boundary. In addition, the average of the observed , which better matches the value of the dataset being used for comparison. Therefore, it's certainly reasonable to use the dataset on 13 March 2012 for the comparison.

The performance of four detection algorithms for the SST dataset observed on 13 March 2012 and 22 March 2012 are shown in Figure 44-46. Here the dataset observed on 13 March 2012 with is simulating Socorro, New Mexico's seeing condition and dataset observed on 22 March 2012 with is simulating Exmouth, Australia's seeing condition.

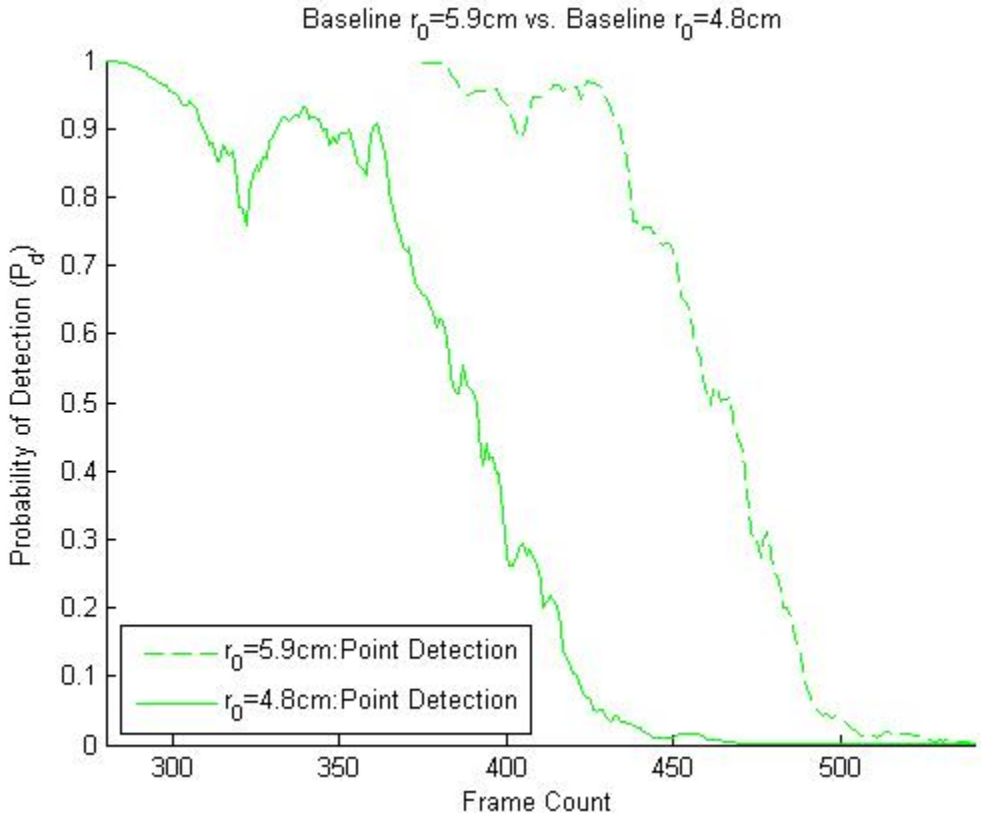

Figure 44. Performance of the baseline detect algorithm with vs. point detection algorithm with .

The performance of the baseline detection algorithms with vs. point detection algorithm with is shown in Figure 44. The result illustrates that the baseline detection algorithm with condition simulating Socorro, New Mexico clearly outperform the point detection algorithm with condition simulating Exmouth, Australia.

Detailed analysis and comparison of algorithm performances are listed in Table 13.

Table 13. Comparison chart for the point detection algorithm with vs. baseline detection algorithm with .

Point Detection dataset with					
Point Detection (Baseline) dataset with					

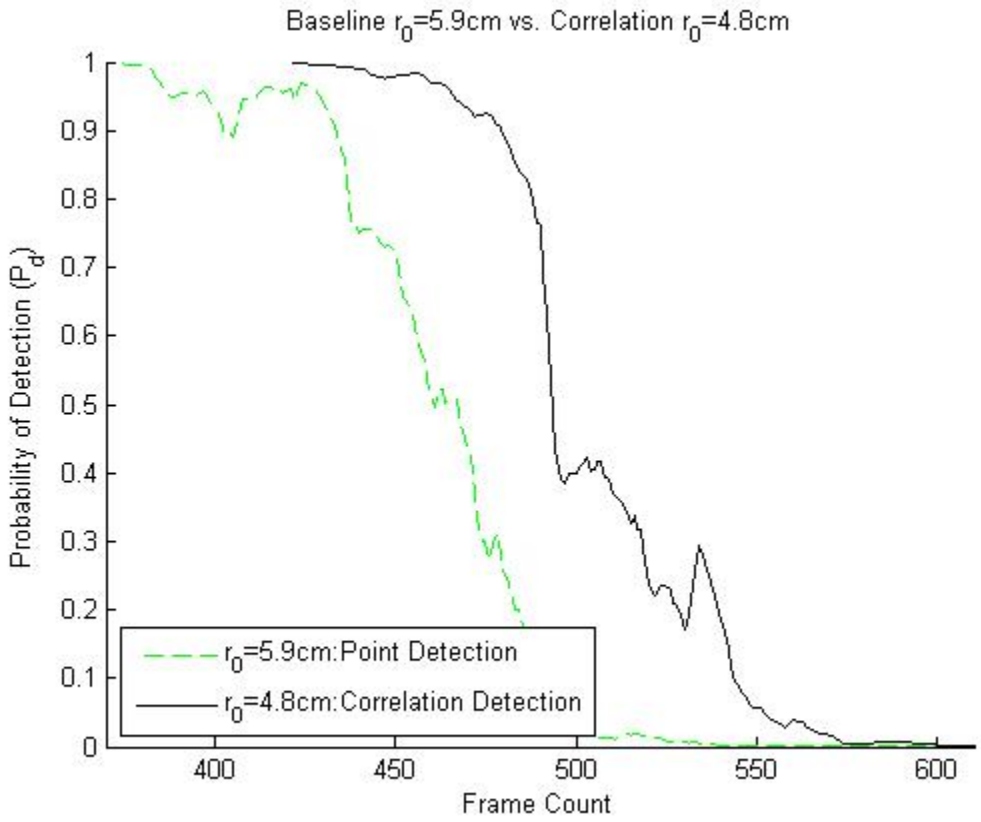

Figure 45. Performance of the **baseline detect algorithm with vs. correlation detection algorithm with .**

The performance of the baseline detection algorithms with vs. correlation detection algorithm with is shown in Figure 44. The result illustrates that the correlation detection algorithm with condition simulating Exmouth, Australia clearly outperform the baseline detection algorithm with condition simulating Socorro, New Mexico.

Detailed analysis and comparison of algorithm performances are listed in Table 14.

Table 14. Comparison chart for the correlation detection algorithm with vs. baseline detection algorithm with .

Correlation Detection dataset with					
Point Detection (Baseline) dataset with					

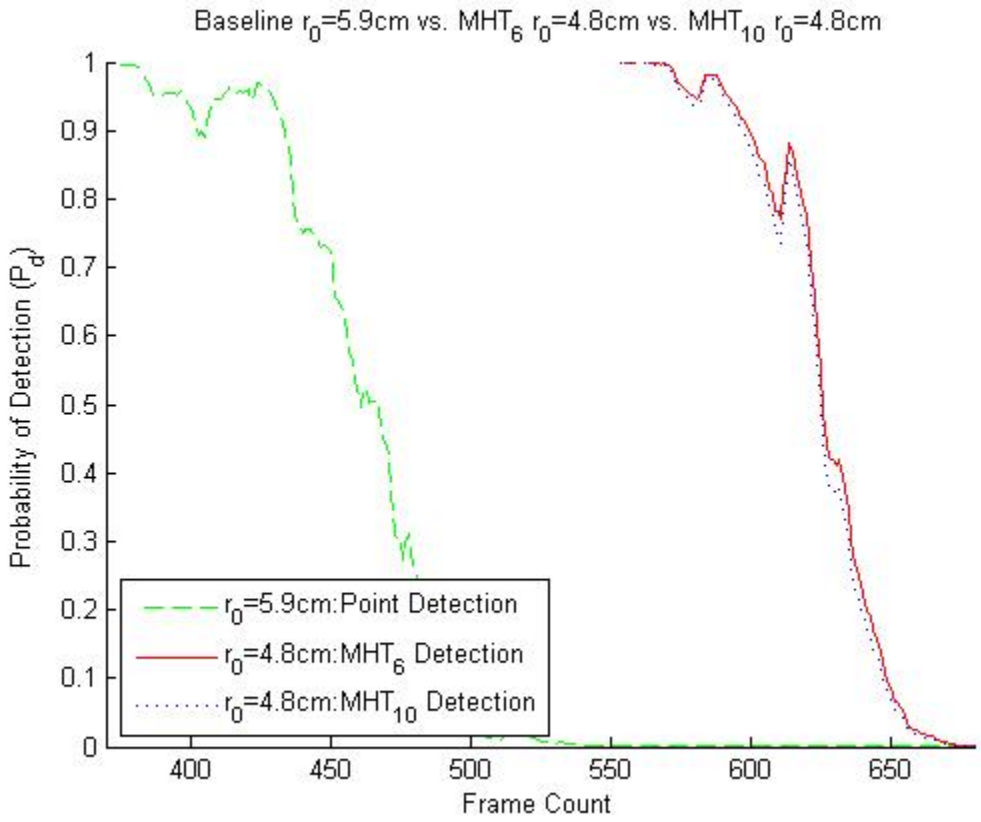

Figure 46. Performance of the b**aseline detect algorithm with vs. MHT_6 and MHT_{10} algorithms with** .

The performance of the baseline detection algorithms with vs. MHT_6 and MHT_{10} with is shown in Figure 44. The result illustrates that the MHT_6 and MHT_{10} algorithms with condition simulating Exmouth, Australia clearly outperforms the baseline detection algorithm with condition simulating Socorro, New Mexico.

Detailed analysis and comparison of algorithm performances are listed in Table 15.

Table 15. Comparison chart for the MHT_6 and MHT_{10} algorithm with vs. baseline detection algorithm with .

MHT_6 dataset with					
MHT_{10} dataset with					
Point Detection (Baseline)					

dataset with					

A conclusion can be made from using Figure 44-46, and Table 13-15, for the performance comparison of detection algorithms. Once SST is relocated to Exmouth, Australia, performance of the baseline will fall by approximately 45%. However, this can be compensated by implementing the correlation detection algorithm. The result indicates that performance of the SST using the correlation detection algorithm at Exmouth, Australia can exceed the SST baseline detection algorithm at Socorro, New Mexico by up to approximately 45%. Furthermore, implementation of the MHT detection algorithms will far exceed current capability of the SST using the baseline by up to approximately 95%.

V. Conclusions and Recommendations

5.1 Conclusions of Research

There is an ongoing effort by the DoD in order to attain a global SSA coverage to satisfy the U.S National Space Policy. This can be accomplished by improving the performance of the optical telescope and strategically placing GBOs for a maximum global coverage. Improving the image processing techniques is a non-material solution, a cost effective method for improving the detection capability of space objects because it avoids costly physical alternations to optical telescope. Although the DoD identified candidate sites for placement of SSTs to support the SSN, actual performance of these sites are currently unknown.

This research presents a method of improving the detection capability of the SST by introducing new detection algorithms on top of the three previously studied, and predicting the performance these detection algorithms in one of the candidate site. Results of this research suggest that the detection algorithm using the MHT is an improvement over the BHT currently used by SST when the object is not centered on a single pixel. However, due to the motion, the object is unlikely to fall in the center pixel, but rather on one of the corner or side pixel, resulting in the MHT that performs better. In four out of six datasets, the MHT_6 outperformed the MHT_{10} due to lower SNR, threshold. But, when the object fell in between two sub-pixels, the MHT_{10} outperformed all other algorithms. Previous studies discovered that the gains in detection performance by the MHT_{10} came at the cost of 600% increase in computing power [28]. However, the M&S revealed that in two out of six cases, the MHT_6 provided nearly equal performance, while only requiring only half of the computing cost of the MHT_{10}. And in four out of six cases, the MHT_6 provided better detection performance, while only requiring only half of the computing cost of the MHT_{10}.

This research sought to predict the performance of the SST in Exmouth, Australia. In the process of producing a result that's more accurate and valid, three discoveries were made. The first discovery identified a more accurate way of measuring the atmospheric seeing condition, . Comparison of numerically calculated and analytically simulated proved that current the method of measuring the seeing parameter by MIT/LL is based on a false assumption. More importantly, the performance of the SST now can be improved using a true atmospheric seeing parameter. The second discovery identified a method of determining the true initial point that's crucial for obtaining an accurate result for performance of the detection algorithms by providing synchronization point. Lastly, the third discovery identified that the object position location and its resulting intensity distribution are two parameters used in the comparison of two different datasets.

The result of comparison revealed that when SST is relocated to Exmouth, Australia, the performance of the baseline detection algorithm is predicted to suffer significantly due to poor seeing conditions. But by implementing the correlation detection algorithm or the MHTs detection algorithms, the lost performance can be bought back. Implementation of the correlation detection algorithm would not only compensate for the loss of the performance, it'll exceed the performance of the baseline detection algorithm at Socorro, New Mexico by up to approximately 45%. Furthermore, implementation of the MHT detection algorithms would improve the current capability of the SST by up to approximately 95%.

The result of the AFIT telescope experiment proved that the analytical model for obtaining valid. It also demonstrated that the MHT_6 and MHT_{10} perform equally at the SST's chosen probability false alarm rate, which validates results of MHTs obtained from the SST eclipse experiment. Additionally, the used for deriving the SNR thresholds for the MHT_6 and

MHT_{10} were validated. The result of the AFIT telescope experiment gives us an ability to test SST algorithms under very poor seeing conditions.

5.2 Recommendations for Future Research

The MHT algorithms provided an improved detection performance. However, this was based on a Gaussian PDF. Future follow-on work to this research could emphasize identifying an appropriate PDF for the MHT using a different number of hypotheses. This would improve the detection performance by providing an accurate SNR, threshold. Additionally, although performance of the SST in Exmouth, Australia was successfully predicted, more analysis must be performed using additional datasets to increase the accuracy and fidelity.

Bibliography

[1] J. C. Zingarelli, "ENHANCING GROUND BASED TELESCOPE PERFORMANCE WITH IMAGE PROCESSING," Air Force Institude of Technology, Wight-Patterson Air Force Base, OH, 2013.

[2] National Aeronautics and Space Administration, "Small Spacecraft Technology State of the Art," Ames Research Center, 2014. [Online]. Available: http://www.nasa.gov/sites/default/files/files/Small_Spacecraft_Technology_State_of_the_Art_2014.pdf. [Accessed 26 August 2014].

[3] "Global Space Programs," Space Foundation, [Online]. Available: http://www.spacefoundation.org/programs/public-policy-and-government-affairs/introduction-space/global-space-programs. [Accessed 26 December 2012].

[4] S. Singh, "The Space Industry: Seriously Congested, Contested And Poised For Growth," Forbes, 2014.

[5] P. Anz-Meador and J.-C. Liou, "Analysis and Consequences of the Iridium 33 - Cosmos 2251 Collision," National Aeronautics and Space Administration, [Online]. Available: http://ntrs.nasa.gov/archive/nasa/casi.ntrs.nasa.gov/20100008433.pdf. [Accessed 18 October 2014].

[6] National Aeronautics and Space Administration, "Chinese Anti-satellite Test Creates Most Severe Orbital," *Orital Debris Quaterly News*, vol. 2, pp. 1-3, 2007.

[7] "2011 Annual Report," Aerospace Corporation, 2011.

[8] United States Government, "Public Law 109-155, NASA Authorization Act 2005," 109th United States Congress, 2005.

[9] P. Martin, "NASAs Efforts to Identify Near-Earth Objects and Mitigate Hazards," NASA Inspector General, 2014.

[10] Office of the President of the United States of America, "NATIONAL SPACE POLICY of the UNITED STATES of AMERICA," United States Government, Washington

DC, 2010.

[11] M. Morton and T. Roberts, "Joint space operations center (JSpOC) mission system (JMS)," DTIC, AIR FORCE SPACE COMMAND PETERSON AFB CO, 2011.

[12] "USSTRATCOM Space Control and Space Surveillance Fact Sheet," USSTRATCOM, Omaha, 2008.

[13] Massachusetts Insitude of Technology Lincoln Laboratory, "Space Surveillance Telescope (SST) Phase I System Test and Demonstration Final Report," DARPA, 2012.

[14] "SST Australia: Signed, Sealed and Ready for Delivery," DARPA, [Online]. Available: http://www.darpa.mil/NewsEvents/Releases/2013/12/06.aspx. [Accessed 20 May 2014].

[15] "Elements," Missile Defense Agency, 31 July 2014. [Online]. Available: http://www.mda.mil/system/sensors.html. [Accessed 30 December 2014].

[16] "Space Situational Awareness," Space Generation Advisory Council, [Online]. Available: http://www.agi.com/resources/educational-alliance-program/curriculum_exercises_labs/SGAC_Space%20Generation%20Advisory%20Council/space_situational_awareness.pdf. [Accessed 20 June 2014].

[17] R. Grant, "Vulnerability in Space," *Air Force Magazine*, vol. 91, no. 6, pp. 24-29, 2008.

[18] "Boeing Surprised by Air Force Cost Estimate for 2nd SBSS," SPACE NEWS, 21 March 2011. [Online]. Available: http://spacenews.com/boeing-surprised-air-force-cost-estimate-2nd-sbss/. [Accessed 10 December 2014].

[19] M. Gruss, "With SBSS Follow-on in Limbo, U.S. Space Surveillance Gap Looms," Space News, 24 Feburary 2014. [Online]. Available: http://www.spacenews.com/article/military-space/39606military-space-quarterly-with-sbss-follow-on-in-limbo-us-space. [Accessed 21 September 2014].

[20] E. Stansbery, "Orbital Debris Program Office," National Aeronautics and Space Administration, 2 October 2012. [Online]. Available: http://orbitaldebris.jsc.nasa.gov/photogallery/beehives.html#geo. [Accessed 26 June 2013].

[21] BAE Systems, "Unique search and track procedures utilizing the Ground-based Electro-Optical Deep Space Surveillance (GEODSS) worldwide sites," in *Advanced Maui Optical and Space Surveillance Technologies Conference*, Maui, 2012.

[22] DARPA, "Space Surveillance Telescope (SST)," Tactical Technology Office, [Online]. Available: http://www.darpa.mil/Our_Work/TTO/Programs/Space_Surveillance_Telescope_(SST).aspx. [Accessed 2013 November 2013].

[23] D. F. Woods, R. Y. Shah, J. A. Johnson, A. Szabo, E. C. Pearce, R. L. Lambour and W. J. Faccenda, "Space Surveillance Telescope: focus and alignment of a three mirror telescope," *Optical Engineering*, vol. 52, no. 2, 2013.

[24] Office of the Press Secretary , "On-the-Record Conference Call on the President's Upcoming Trip to Asia," 15 November 2012. [Online]. Available: http://www.whitehouse.gov/the-press-office/2012/11/15/record-conference-call-presidents-upcoming-trip-asia. [Accessed 19 November 2014].

[25] M. E. Manyin, S. Daggett, B. Dolven, S. V. Lawrence, M. F. Martin, R. O'Rourke and B. Vaughn, "Pivot to the Pacific? The Obama Administration's "Rebalancing" Toward Asia," Congressional Research Service, 2012.

[26] W. Kilar, "SMC/SY Analysis of Ground-Based Optical Systems," Space and Missile Systems Center, LAAFB, El Segundo, 2014.

[27] G. S. F. S. M. B. a. J. S. H. Viggh, "Applying Electro-Optical Space Surveillance Technology to Asteroid Search and Detection: The Linear Program Results," in *Space Control Conference*, Lexington, 1998.

[28] J. B. Evans and others, "Detection and Discovery of Near-Earth Asteroids by the LINEAR Program," *Lincoln Laboratory Journal*, vol. 14, no. 2, pp. 199-220, 2003.

[29] J. C. Zingarelli, "Enhancing Ground Based Telescope Performance With Image Processing," Air Force Institude of Technology, Wight-Patterson Air Force Base, 2013.

[30] S. C. Pohlig, "An Algorithm for Detection of Moving Optical Targets," *IEEE Transactions on Aerospace and Electronic Systems*, vol. 25, no. 1, pp. 56-63, 1989.

[31] A. O'Dell, "DETECTING NEAR-EARTH OBJECTS USING CROSS-CORRELATION WITH A POINT SPREAD FUNCTION," Air Force Institude of Technology, Wright-Patterson Air Force Base, Ohio, 2009.

[32] A. O'Dell and S. Cain, "Investigating the Effects of Atmospheric Seeing on the Detection of near Earth Orbiting Asteroids," in *IEEE Aerospace Conference,* 2009.

[33] J. W. Goodman, Introduction to Fourier Optics, 3rd ed., Englewood, Co,: Roberts & Company, 2005.

[34] R. J. Noll, "Zernike polynomials and atmospheric turbulence," *JOsA,* vol. 66, no. 3, 1976.

[35] M. Richmond, "Atmospheric effects: extinction and seeing," Rochester Institude of Technology, 2014. [Online]. Available: http://spiff.rit.edu/classes/phys445/lectures/atmos/atmos.html. [Accessed December 2013].

[36] "Atmospheric Effects - Seeing," Australia Telescope National Facility, 2 January 2014. [Online]. Available: http://www.atnf.csiro.au/outreach/education/senior/astrophysics/atmosphere.html. [Accessed 10 Dec 2013].

[37] K. P. Vitayaudom, "Analysis of Non-Uniform Gain for Control of a Deformable Mirror in an Adaptive-Optics System," AFIT, WPAFB, OH, 2008.

[38] G. Kirchner, D. Kucharski, F. Koidl and J. Weingrill, "Measuring Atmospheric Seeing with kHz SLR," [Online]. Available: http://cddis.gsfc.nasa.gov/lw15/docs/papers/Measuring%20Atmospheric%20Seeing%20with%20KHz%20SLR.pdf. [Accessed 30 July 2014].

[39] J. W. Goodman, Statistical optics, New York: Wiley-Interscience, 1985.

[40] L. C. Andrews and R. L. Phillips, Laser beam propagation through random media Vol. 10. No. 3.626196, Bellingham: SPIE press, 2005.

[41] "Satellite dish pointing angle calculator," Satellite Signals, 23 May 2014. [Online]. Available: http://www.satsig.net/maps/satellite-tv-dish-pointing-australia-new-zealand.htm. [Accessed 20 December 2014].

[42] C. J. R. Peterson, "NEAR EARTH OBJECT DETECTION USING A POISSON STATISTICAL," Air Force Institute of Technology, Wright-Patterson Air Force Base, OH, 2012.

[43] I. B. Putnam and S. C. Cain, "Modeling a Temporally Evolving Atmosphere with Zernike Polynomials," in *Advanced Maui Optical and Space Surveillance Technologies Conference*, Maui, 2012.

[44] F. J. Vrba, M. E. DiVittorio, R. B. Hindsley, H. R. Schmitt, J. T. Armstrong, P. D. Shankland, D. J. Hutter and J. A. Benson, "A SURVEY OF GEOSYNCHRONOUS SATELLITE GLINTS," DTIC, Flagstaff, 2009.

[45] J. D. Schmidt, Numerical simulation of optical wave propagation with examples in MATLAB, Washington: SPIE, 2010.

REPORT DOCUMENTATION PAGE			Form Approved OMB No. 074-0188
The public reporting burden for this collection of information is estimated to average 1 hour per response, including the time for reviewing instructions, searching existing data sources, gathering and maintaining the data needed, and completing and reviewing the collection of information. Send comments regarding this burden estimate or any other aspect of the collection of information, including suggestions for reducing this burden to Department of Defense, Washington Headquarters Services, Directorate for Information Operations and Reports (0704-0188), 1215 Jefferson Davis Highway, Suite 1204, Arlington, VA 22202-4302. Respondents should be aware that notwithstanding any other provision of law, no person shall be subject to an penalty for failing to comply with a collection of information if it does not display a currently valid OMB control number. **PLEASE DO NOT RETURN YOUR FORM TO THE ABOVE ADDRESS.**			
1. REPORT DATE *(DD-MM-YYYY)* 26-03-2015	**2. REPORT TYPE** Master's Thesis		**3. DATES COVERED** *(From – To)* March 2014 – March 2015
TITLE AND SUBTITLE Improving the Performance of the Space Surveillance Telescope as a Function of Seeing Parameter			**5a. CONTRACT NUMBER** **5b. GRANT NUMBER** **5c. PROGRAM ELEMENT NUMBER**
6. AUTHOR(S) Jeon, Jae H, Captain, USAF			**5d. PROJECT NUMBER** 15G122 **5e. TASK NUMBER** **5f. WORK UNIT NUMBER**
7. PERFORMING ORGANIZATION NAMES(S) AND ADDRESS(S) Air Force Institute of Technology Graduate School of Engineering and Management (AFIT/EN) 2950 Hobson Way, Building 640 WPAFB OH 45433-8865			**8. PERFORMING ORGANIZATION REPORT NUMBER** AFIT-ENG-MS-15-M-050
9. SPONSORING/MONITORING AGENCY NAME(S) AND ADDRESS(ES) Dr. Linday Millard (email: lmillard@rand.org) Phone:(571) 218-4354 DARPA/TTO DEF ADVANCED RESEARCH PROJECTS AGCY (HR0011) 675 NORTH RANDOLPH STREET ARLINGTON, VA, 22203-2114, US			**10. SPONSOR/MONITOR'S ACRONYM(S)** DARPA **11. SPONSOR/MONITOR'S REPORT NUMBER(S)**
12. DISTRIBUTION/AVAILABILITY STATEMENT **DISTRUBTION STATEMENT A.** APPROVED FOR PUBLIC RELEASE; DISTRIBUTION UNLIMITED.			
13. SUPPLEMENTARY NOTES This material is declared a work of the U.S. Government and is not subject to copyright protection in the United States.			
14. ABSTRACT This research paper investigates ways to improve the detection capability and predict the performance of the Space Surveillance Telescope (SST) system when it's relocated to Exmouth, Australia. The dataset collected by the SST observing the Geosynchronous Earth Orbit (GEO) satellite, ANIK-F1, entering the earth's eclipse is used to test the performance of the three existing and one new detection algorithm. The three existing algorithms are the point detection (Binary Hypothesis Test (BHT)), correlation detection (CD-BHT), and Multi-hypothesis Test using ten hypotheses (MHT10), and the new detection algorithm is the Multi-hypothesis Test using six hypotheses (MHT6). To improve the accuracy and validness of the comparison, a new method of obtaining the true atmospheric seeing parameter, terminator (point before the object entering the eclipse), and parameters used for the comparison are also investigated. It is found that the MHTs vastly outperform the BHTs, and the MHT6 offers a similar or improved performance over the MHT10, but requiring only half of the computing power			
15. SUBJECT TERMS Multi-hypotheses Test, Binary Hypotheses Test, , Remote Sensing, Space Surveillance Telescope, Atmospheric Seeing Parameter,			

16. SECURITY CLASSIFICATION OF:			**17. LIMITATION OF ABSTRACT**	**18. NUMBER OF PAGES**	**19a. NAME OF RESPONSIBLE PERSON** Cain, Stephen C., Civ, USAF, (ENG)
a. REPORT **U**	**b. ABSTRACT** **U**	**c. THIS PAGE** **U**	**UU**	110	**19b. TELEPHONE NUMBER** *(Include area code)* (937) 255-3636, x 4716 (Stephen.Cain@afit.edu)